

Water Resources Research



RESEARCH ARTICLE

10.1029/2022WR032314

Key Points:

- · Numerical experiments show droughts enhance vertical CO2 export to the atmosphere, whereas storms promote lateral carbon export into streams
- Carbonate precipitation reduces inorganic carbon (IC) in water under dry conditions while dissolution adds IC in water under wet conditions
- Subsurface structures exert smaller influence on the rates of carbon transformation and chemical weathering than hydrological conditions

Supporting Information:

Supporting Information may be found in the online version of this article.

Correspondence to:

lili@engr.psu.edu

Citation:

Wen, H., Sullivan, P. L., Billings, S. A., Ajami, H., Cueva, A., Flores, A., et al. (2022). From soils to streams: Connecting terrestrial carbon transformation, chemical weathering, and solute export across hydrological regimes. Water Resources Research. 58, e2022WR032314. https://doi. org/10.1029/2022WR032314

Received 5 MAR 2022 Accepted 6 JUN 2022

This is an open access article under the terms of the Creative Commons distribution and reproduction in any

© 2022. The Authors.

Attribution License, which permits use, medium, provided the original work is properly cited.

From Soils to Streams: Connecting Terrestrial Carbon Transformation, Chemical Weathering, and Solute Export **Across Hydrological Regimes**

Hang Wen^{1,2} D, Pamela L. Sullivan³ D, Sharon A. Billings⁴ D, Hoori Ajami⁵ D, Alejandro Cueva⁶ D, Alejandro Flores⁷, Daniel R. Hirmas⁵, Aaron N. Koop⁸, Katie Murenbeeld⁷, Xi Zhang⁹, and Li Li²

¹Institute of Surface-Earth System Science, School of Earth System Science, Tianjin University, Tianjin, China, ²Department of Civil and Environmental Engineering, Pennsylvania State University, University Park, PA, USA, 3College of Earth, Ocean, and Atmospheric Science, Oregon State University, Corvallis, OR, USA, 4Department of Ecology and Evolutionary Biology, Kansas Biological Survey & Center for Ecological Research, University of Kansas, Lawrence, KS, USA, 5Department of Environmental Sciences, University of California, Riverside, CA, USA, 6Departamento de Ciencias de la Sustentabilidad, El Colegio de la Frontera Sur, Unidad Villahermosa, Tabasco, Mexico, ⁷Department of Geosciences, Boise State University, Boise, ID, USA, 8Department of Geography and Atmospheric Science, University of Kansas, Lawrence, KS, USA, ⁹Agricultural Center, Louisiana State University, Bossier City, LA, USA

Abstract Soil biota generates carbon that exports vertically to the atmosphere (CO₂) and transports laterally to streams and rivers (dissolved organic and inorganic carbon, DOC and DIC). These processes, together with chemical weathering, vary with flow paths across hydrological regimes; yet an integrated understanding of these interactive processes is still lacking. Here we ask: How and to what extent do subsurface carbon transformation, chemical weathering, and solute export differ across hydrological and subsurface structure regimes? We address this question using a hillslope reactive transport model calibrated using soil CO₂ and water chemistry data from Fitch, a temperate forest at the ecotone boundary of the Eastern temperate forest and mid-continent grasslands in Kansas, USA. Model results show that droughts (discharge at 0.08 mm/day) promoted deeper flow paths, longer water transit time, carbonate precipitation, and mineralization of organic carbon (OC) into inorganic carbon (IC) (~98% of OC). Of the IC produced, ~86% was emitted upward as CO₂ gas and ~14% was exported laterally as DIC into the stream. Storms (8.0 mm/day) led to carbonate dissolution but reduced OC mineralization (~88% of OC) and promoted DOC production (~12% of OC) and lateral fluxes of IC (~53% of produced IC). Differences in shallow-versus-deep permeability contrasts led to smaller difference (<10%) than discharge-induced differences and were most pronounced under wet conditions. High permeability contrasts (low vertical connectivity) enhanced lateral fluxes. Model results generally delineate hillslopes as active CO₂ producers and vertical carbon transporters under dry conditions, and as active DOC producers and lateral carbon transporter under wet conditions.

1. Introduction

Soil is the largest terrestrial carbon pool (Batjes, 2014). Vertical fluxes of CO₂ into the atmosphere have been extensively studied (e.g., Bond-Lamberty et al., 2020; Chapin et al., 2006; Jian et al., 2021). Lateral fluxes of dissolved organic and inorganic carbon (DOC and DIC) from terrestrial to aquatic systems have been increasingly recognized for emitting substantial amounts of CO₂ along river corridors (e.g., Barnes et al., 2018; Battin et al., 2009; Regnier et al., 2013). Vertical and lateral carbon fluxes, however, are often studied separately within disciplinary boundaries (Brookfield et al., 2021; Grimm et al., 2003). Their connections, partitioning, and relationship to carbon transformation across gradients of hydroclimatic and subsurface conditions have remained poorly understood. As a result, quantifications of carbon transformation rates and fluxes have remained highly uncertain (Duvert et al., 2018).

Organic carbon (OC) transformation and chemical weathering (i.e., carbonate dissolution and precipitation) are key processes that produce dissolved and gaseous carbon and drive terrestrial carbon dynamics. Their rates depend on hydroclimatic conditions (Figure 1) that are bound to change under future climates with intensifying hydrological extremes including droughts and storms (Ault, 2020; Mastrotheodoros et al., 2020). Soil respiration rates often increase with temperature (Lloyd & Taylor, 1994) but peak at 50%–70% water saturation (Yan et al., 2018).

WEN ET AL. 1 of 26

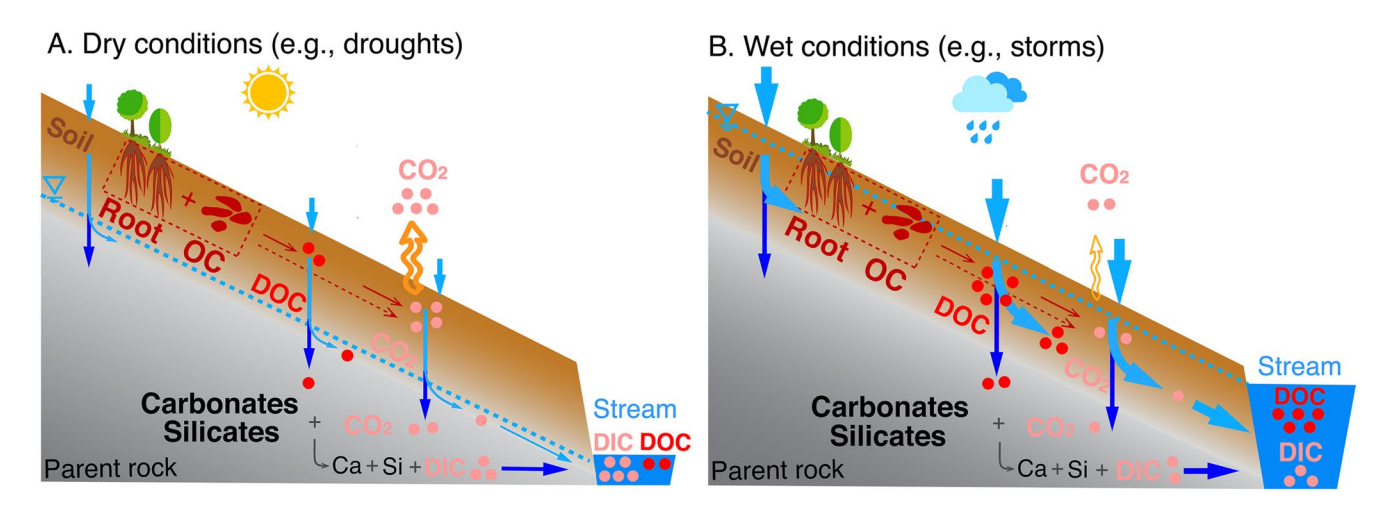


Figure 1. Conceptual diagrams of reactions and fluxes under dry and wet conditions. (a) Under dry conditions (e.g., droughts), deeper flow paths (dashed blue lines), slower flow (thin blue arrows), and longer water transit times promote soil $CO_2(g)$ production and vertical carbon export to the atmosphere (yellow arrows) but reduce lateral export of dissolved organic carbon (DOC) and dissolved inorganic carbon (DIC) via shallow and deeper groundwater flow paths. (b) Under wet conditions (e.g., storms), shallow flow paths and fast flow in OC-rich soils (thick blue arrows) and shorter water transit times reduce carbon mineralization, soil $CO_2(g)$ production, and vertical CO_2 fluxes but promote lateral carbon fluxes to streams and rivers.

Overly wet conditions can induce anoxic conditions and limit soil respiration (Vasconcelos et al., 2004); overly dry conditions, although with abundant oxygen, can limit microbial metabolism and reduce respiration rates by increasing physical protection of OC and reducing carbon-enzyme contact (Li, Maher, et al., 2017). Droughts can also induce anaerobic metabolism and hypoxic conditions, especially in headwater streams (Gómez-Gener et al., 2020).

Hydrological events and flow regimes regulate flow paths and solute export from terrestrial to aquatic systems. Large storms enhance land-river hydrological connectivity and mobilize stored DOC (Raymond & Saiers, 2010; Wen et al., 2020). Riverine DOC concentrations increase with river discharge in approximately 80% of watersheds in the U.S. (Zarnetske et al., 2018). Wetter conditions and resultant predominance of shallow soil water flow often facilitates the export of solutes enriched in shallow soils. Soil water charged with high CO₂ and DOC

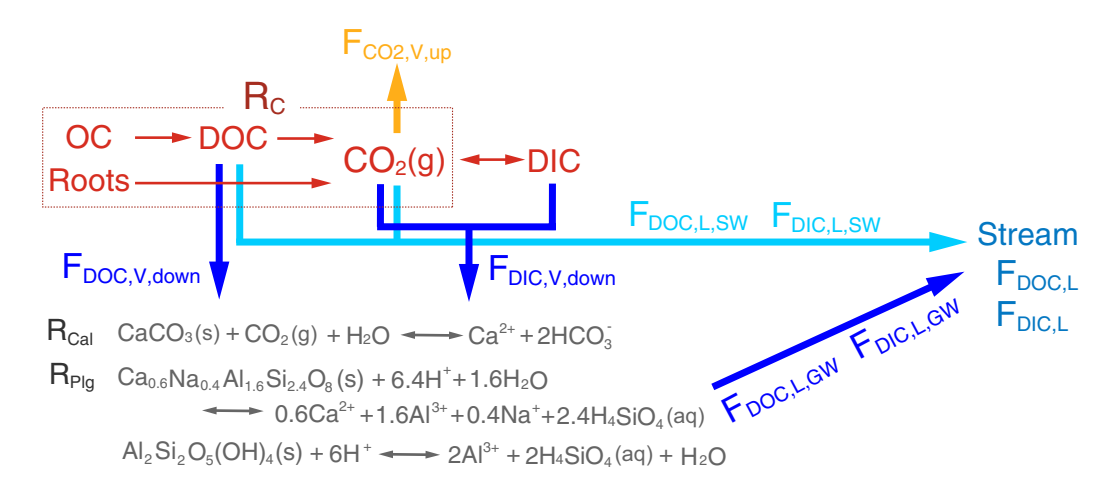


Figure 2. Reactions (red arrows) and fluxes (blue and yellow arrows) considered in this work. The reactions include soil respiration (root respiration and microbial OC mineralization) to produce dissolved inorganic carbon (DIC), $CO_2(g)$, and dissolved organic carbon (DOC). Gaseous CO_2 can vertically emit to the atmosphere ($F_{CO_2,V,up}$), dissolve in water to become DIC, or precipitate to become carbonate minerals. Dissolved carbon (DIC and DOC) can flow laterally via shallow water path (SW, $F_{DOC,L,SW}$, $F_{DIC,L,SW}$), entering streams via a shorter path with shorter transit time, or vertically recharge to the depth and eventually enter streams via groundwater (GW) discharge via a longer flow path. Note that $F_{DIC,L} = F_{DIC,L,SW} + F_{DIC,L,GW}$, and $F_{DOC,L} = F_{DOC,L,SW} + F_{DOC,L,GW}$. Detailed reactions and reaction rate laws are in Table 1 and Text S2 in Supporting information S1.

WEN ET AL. 2 of 26



can also recharge more into the deeper subsurface under wet conditions, thereby enhancing weathering and DIC lateral fluxes (Clow & Mast, 2010; Wen et al., 2021). In contrast, droughts reduce DOC export not only by reducing water fluxes but also by drought-induced acidification and decreasing DOC solubility (Clark et al., 2010). Under dry conditions, streams are often sustained by deeper groundwater flow that is characterized by low DOC and elevated geogenic solutes.

Subsurface flow paths and solute export also depend on subsurface physical structures, particularly the vertical distribution of permeability over depth, or vertical connectivity (Figure 1). Permeability typically decreases with depth following an exponential- or power-law form (Cardenas & Jiang, 2010; Saar & Manga, 2004). Soil permeability is generally orders-of-magnitude higher than that of weathered or parent rocks at depth (Welch & Allen, 2014), leading to water fluxes that sharply decrease with depth (Harman & Cosans, 2019). The vertical distribution of permeability therefore regulates water flow partitioning via shallow versus deep paths and new and old water transit times (Harman & Sivapalan, 2009; Sprenger et al., 2018; Xiao et al., 2021). Subsurface structure and shallow versus deeper water partitioning is often reflected in stream chemistry, as older waters from deeper subsurface often carry highly concentrated weathering products such as silica and cations (Benettin et al., 2015; Torres & Baronas, 2021), whereas younger waters are often enriched with solutes that are abundant in shallow soils (Benettin et al., 2020; Li et al., 2021).

The linkage between subsurface flow paths and reactions, including soil carbon transformation and chemical weathering at depth, however, is generally poorly understood. Soil CO₂ effluxes are typically quantified using localized, small-scale CO₂ vertical fluxes measured at ground surface (Barba et al., 2018; Carey et al., 2016; Kuzyakov, 2006; Richter & Billings, 2015). Concerted measurements of DIC, ¹³C isotopes, and instantaneous river discharge have revealed the connections between source waters (shallow soil water and deeper groundwater) and their delivery to streams (Duvert et al., 2020; Horgby, Boix Canadell, et al., 2019; Horgby, Gómez-Gener, et al., 2019). The entangled interactions among multiple factors however challenge the differentiation of individual effects. We generally lack an integrated view on the connections and regulation of soil respiration and chemical weathering and solute and gas export fluxes.

Here we begin to address this knowledge gap by asking the question: *How and to what extent do subsurface carbon transformation, chemical weathering, and solute export differ across hydrological and subsurface structure regimes?* To answer this question, we draw upon the rich foundation of reactive transport modeling (RTM) that has been widely used to understand hydrological and biogeochemical coupling (Ackerer et al., 2021; Dwivedi et al., 2022; Jung & Navarre-Sitchler, 2018; Li, Bao, et al., 2017; Wen et al., 2020). Here we first developed a hillslope-scale RTM using soil CO₂ and soil water chemistry data from the Fitch Forest, a temperate forest at the ecotone boundary of the Eastern temperate forest and mid-continent grasslands in Kansas (Fitch, 2006). We then fixed reaction parameters and conditions at Fitch (e.g., hillslope topography, organic carbon content, mineralogy) and carried out numerical experiments by varying conditions across hydrological extremes from droughts to storms (mean discharge from 0.08 to 8.0 mm/day) in three scenarios of shallow-versus-deep permeability contrasts. By doing so we can differentiate and quantify the impacts of hydrological conditions and permeability contrasts on reactions and solute export.

2. Research Site, Field Measurements, and Data

The Fitch Forest (hereafter Fitch) at the University of Kansas Field Station (Figure 3) is located at the ecotone boundary of the Eastern temperate forest and mid-continent grasslands in Kansas. The mean annual temperature and precipitation are 13.3°C and 945 mm, respectively. The majority of rainfall occurs in the spring and summer (Brunsell & Wilson, 2013). The elevation ranges from 274 to 326 m and slope from 2.0% to 57.5%. The bedrock is mainly composed by the Upper and Middle Pennsylvania limestone, sandstone, and shale (Ashok & Sophocleous, 2008; Dickey et al., 1977). At an ecotone boundary, Fitch is highly sensitive to climate conditions; relatively small decreases in mean annual precipitation could push the system to more savannah-like land cover. The observed daily range of mean discharge at Fitch varies from 0.04 to 8.3 mm/day.

Fitch has extensive measurements of soil properties, water table, and water chemistry data. We specifically focused on a planar hillslope covered by temperate forests to reduce topographic complexity; dominant vegetation is composed of mature oak (*Quercus* spp.), hickory (*Carya* spp.), elm (*Ulmus americana*), white ash (*Frax*-

WEN ET AL. 3 of 26

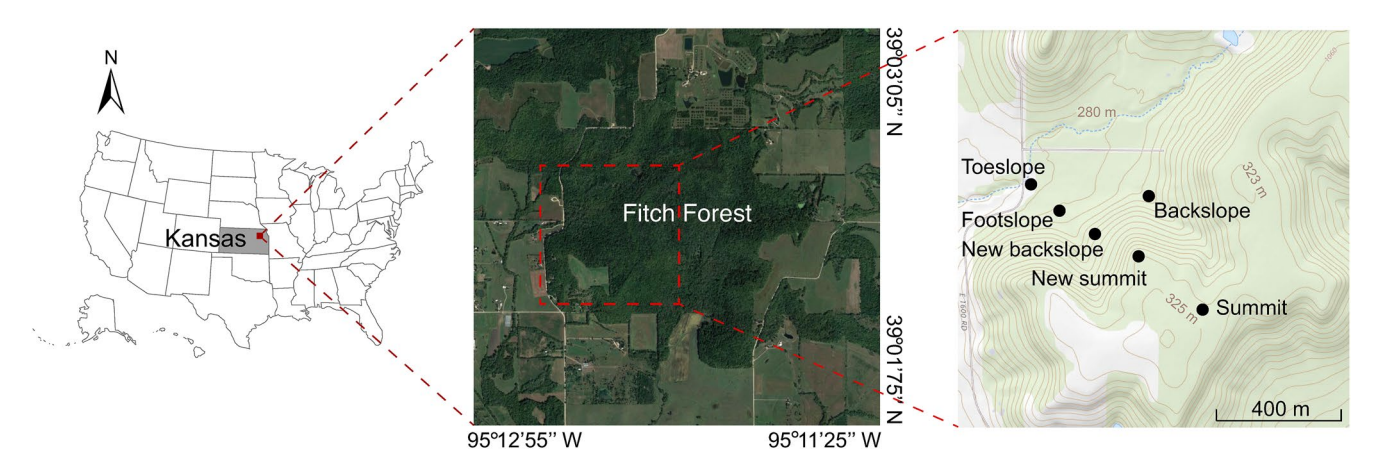


Figure 3. Location of the study site. Subsurface characterization data of physical and chemical properties from four hillslope locations (summit, backslope, footslope, and toeslope) were used for model setup. To better align the transect, two of the piezometers (backslope and summit) were moved to different locations on the topographic position, labeled "New Backslope" and "New Summit."

inus americana), trees with walnut (*Juglans nigra*), hackberry (*Celtis occidentalis*), and other hardwood species contributing some canopy cover. Data from four hillslope positions (summit, backslope, footslope, and toeslope) encompass the variations across the entire hillslope and were used in RTM, as detailed later.

Soils at these four topographic positions were excavated, described, and sampled by the Natural Resources Conservation Service (NRCS) to a depth of 1 m. The soil order is Mollisols in general while soils at the summit, backslope, and footslope/toeslope were mapped as the Oska series (Vertic Argiudolls), Rosendale (Typic Eutrudepts)-Bendena (Lithic Hapludolls) complex, and Martin series (Aquertic Argiduolls), respectively (Soil Survery Staff, 2022). Soils at all locations were classified as silty clay loam (Soil Survery Staff, 2010), with an average proportion of ~42.4% clay, 52.8% silt, and 4.8% sand (Table S1 in Supporting Information S1). Soil porosity decreases from ~0.57 at surface to ~0.43 at a depth of 1.0 m.

We used soil CO₂ data from the National Ecological Observatory Network at depths of 10, 40, and 120 cm in the mineral soil along an adjacent hillslope transect. These data were collected at the same time period as the soil water samples. To quantify the water-extractable organic carbon (EOC), soils were collected using a bucket auger and segmented in 10 cm depth intervals. EOC contains a suite of carbon-rich compounds, including organic acids, important biotic weathering agents (Herbert & Bertsch, 1995), as well as compounds with a high potential of undergoing microbial mineralization to CO₂ (Buscot & Varma, 2005) (more details in Supporting Information S1).

Hydrologic conditions were quantified using PVC piezometers installed at all hillslope positions to a depth of $\sim 160~\rm cm$ (small variations exist in installation depth due to varied depth of augur refusal). Two of the piezometers were immediately adjacent to the soil pits (toeslope and footslope) while two were moved to different locations on the topographic position to better align the transect (backslope and summit; see sites labeled "New Backslope" and "New Summit" in Figure 3). The water table elevations and water chemistry in the piezometers were measured weekly or after precipitation events, an approach also implemented for soil water chemistry measurements using ceramic suction cup lysimeters (SK-20s Meter with $\sim 1.0\%$ uncertainties, at depths 30, 60, and 90 cm). Water samples were filtered using 0.45 μ m nylon syringe filters. Alkalinity and major cations (e.g., Ca) were analyzed using an auto-titrator and an inductively coupled plasma optical emission spectroscopy ($\sim 1.0\%$ –5.0% uncertainties), respectively.

The rainfall chemistry was based on data from the National Atmospheric Deposition Program (nadp.sws.uiuc.edu) and from Konza Prairie (lter.konza.ksu.edu/station-keywords/precipitation-chemistry), the closest data site from Fitch (~145 km west). The rainfall has a pH of 6.1, with DOC, DIC, Ca, Na, $H_4SiO_4(aq)$, Al, and Cl^- at 60.0, 12.0, 38.0, 78.0, 10.0, 0.2, and 10.0 µmol/L, respectively. The initial soil water was set in the model using the averaged soil water concentrations, which has a pH of 7.0, with DOC, DIC, Ca, Na, $H_4SiO_4(aq)$, Al, and Cl^- at 2.0×10^{-4} , 7.0×10^{-4} , 5.0×10^{-4} , 1.0×10^{-4} , 3.0×10^{-4} , 1.0×10^{-9} , and 1.0×10^{-4} mol/L, respectively.

WEN ET AL. 4 of 26



3. Hillslope Reactive Transport Model

3.1. The Model Setup

3.1.1. Governing Equations

A two-dimensional (2D) hillslope RTM was set up using the code CrunchTope (Steefel et al., 2015). CrunchTope has been extensively used in understanding chemical weathering, biogeochemical reactions, and physical property evolution (Deng et al., 2017; Druhan et al., 2021; Jung & Navarre-Sitchler, 2018; Lawrence et al., 2014; Li et al., 2010; Maher et al., 2006; Xiao et al., 2021). These applications use 1D or 2D rectangular domains except that Xiao et al. (2021) also adopt a hillslope model. The code integrates advective and diffusive/dispersive transport and biogeochemical reactions. For a representative solute *i*, it solves the following mass conservation equations,

$$\frac{\partial}{\partial t} (\phi C_i) = \nabla \cdot \{\phi \mathbf{D}_i \nabla C_i - \mathbf{u} C_i\} + r_i \tag{1}$$

where ϕ is porosity, C_i is the concentration of solute i (mol/m³ water), D_i is the hydrodynamic dispersion tensor (m² porous media/s), u is the Darcy flow velocity (m³ water/m² porous media/s), and r_i is the reaction rate (mol/m³ water/s) described further in Section 3.2.

3.1.2. Domain Setup

The 2D hillslope domain $(450.0 \times 58.0 \text{ m})$ was set up using the average slope (6.5°) of the Fitch hillslope. The spatial resolution was 4.5 and 0.5 m in the horizontal and vertical directions, respectively. We assumed that the soil and substratum extended through the upper 3.0 m based on observations at the site. Below 3.0 m, the subsurface generally consists of weathered bedrock (3.0-6.0 m) and parent rock (below 6.0 m), which often harbors the groundwater (GW).

3.1.3. Subsurface Physical Properties and Flow Field

The porosity-depth relationship in the top 6.0 m was assumed to follow the exponential function $\phi = \phi_0 e^{-\alpha_{\phi}}$ (Gleeson et al., 2016), where ϕ_0 is the porosity at the ground surface and α_{ϕ} quantifies the steepness of the porosity gradient. Values of ϕ_0 and α_{ϕ} were estimated to be 0.53 and 0.17, respectively (Figure 4a1), based on soil porosity data in the top 1.0 m (Table S1 in Supporting Information S1) and an assumed value of 0.2 at 6.0 m for typical parent rocks. The porosity below 6.0 m (i.e., parent rocks) was assumed to be constant at 0.2.

The permeability in the top 6.0 m was prescribed using the widely used power law function $\kappa = \kappa_0 z^{b_{\kappa}}$ (Cardenas & Jiang, 2010; Saar & Manga, 2004), where κ_0 is the intrinsic permeability (m²) at the ground surface, z is the depth from the ground surface (m), and b_{κ} is the power law exponent that quantifies the steepness of the permeability gradient. The values of κ_0 and b_{κ} were estimated to be 1.7×10^{-11} m² and -0.4, respectively (Figure 4a2), based on the averages of soil permeability in the top 1.0 m calculated from porosity data using the Kozeny-Carman equation (Carman, 1997; Rawls et al., 1998) and an assumed value of 10^{-12} m² at 6.0 m for parent rocks. This is consistent with field observations that permeability contrast between the shallow soil and parent bedrock is about 1–3 orders of magnitude (Elhakim, 2016). The parent rock permeability below 6.0 m was kept constant at 10^{-12} m².

The model assumes that all water entering the soil eventually leaves as discharge. The mean annual discharge at Fitch is 0.8 mm/day (or 0.3 m/a), essentially the difference between mean annual precipitation (2.6 mm/day) and evapotranspiration (1.8 mm/day). The average water table depth (WTD) in the soil was estimated to be 1.5 m at the discharge of 0.8 mm/day (Figure S1 in Supporting Information S1). The unsaturated–saturated interface was prescribed in the model as the depth of WTD. In the unsaturated zone (i.e., above WTD), the vertical flow rate was assumed to equal the infiltration rate (0.8 mm/day) with zero lateral flow. In the saturated zone, the flow field was calculated based on Darcy's law following the permeability distribution. As will be detailed in Section 3.3, water table depth was assumed to vary with discharge to mimic the rising and falling water tables under wet and dry conditions.

WEN ET AL. 5 of 26



3.1.4. Subsurface Biogeochemical Properties

The abundance of OC and roots typically decreases exponentially with depth (Murphy et al., 2019), with the volume percentage (v/v) of OC and roots following the exponential function $VF_{OC} = VF_{OC,0}e^{-\alpha_{oc}}$, where $VF_{OC,0}$ is the average volume fraction at the ground surface. This value was set at 0.04 based on the measured root/soil volume ratio (0.01–0.05) and the typical OC content of 0.01–0.07 in forest soils (Foth, 1978; Sorenson et al., 2020). The coefficient α_{oc} quantifies the steepness of the decline with depth; it was set at -0.5 following the observations that the totals of OC and roots in the second meter are $\sim 50\%$ of that in the top meter of forested soils (Jobbagy & Jackson, 2000). Similarly, biomass was assumed to be $\sim 5 \times 10^{-5}$ (v/v) in the soil surface (Michelsen et al., 2004) and decreased exponentially to $\sim 10^{-7}$ (v/v) at the weathered rock–parent rock interface (6.0 m). Below this interface, OC and root volumes were assumed constant and two-orders-of-magnitude lower than those at the ground surface (Billings et al., 2018). Soil water chemistry indicates that the mineralogy is primarily calcite and plagioclase (Figure S2 in Supporting Information S1). Calcite increased with depth from zero (volume fraction) in soils to 0.10 (v/v) in the parent rock. Plagioclase was assumed constant (0.22, v/v), based on reported mineral volumes in Kansas (Dickey et al., 1977; Ransom et al., 1998).

3.2. Reaction Network and Rate Laws

The biotic reactions include OC decomposition and root respiration (Figure 2 and Table 1). OC is transformed into DOC and CO_2 through microbial activities (Reactions 1–2). Roots can respire to produce CO_2 (Reaction 3); they can also release exudates as DOC, the mineralization of which releases CO_2 (Ekblad & Högberg, 2001; Jones et al., 2004). We do not have data to differentiate these detailed reaction mechanisms so Reaction 3 represents the "bulk" CO_2 production from roots (i.e., root respiration + mineralization of associated root exudates). The organic carbon has three forms in the model: soil OC, microbial community represented as $C_5H_7O_2N$, and DOC (Ahrens et al., 2015; Riley et al., 2014). Produced CO_2 can become $CO_2(g)$ when reaching solubility (Reaction 5) and emit to the atmosphere (Reaction 4); dissolved CO_2 is DIC, the sum of $CO_2(aq)$, HCO_3^- , and CO_3^{2-} (Reactions 6–7). The dissolution of CO_2 acidifies water and accelerates weathering (Reactions 9–11). Produced DOC can sorb on solid surfaces (Reaction 8), which affects its availability for mineralization. The reaction parameters were calibrated by reproducing water chemistry data (Sections 3.3 and 4.1).

Produced $CO_2(g)$ can emit vertically to the atmosphere, which is represented by a "diffusion" or "release" rate $r_{D,CO_2(g)} = D_{CO_{2(g)}} A \left(1 - \frac{c_{CO_{2(g)}}}{k_{eq,4}}\right)$. Here $C_{CO_2(g)}$ is the soil CO_2 gas concentration, and $K_{eq,4}$ (4 × 10⁻⁴ atm) represents the atmospheric CO_2 level. That is, diffusion only occurs when soil $CO_2(g)$ concentration is higher than the atmospheric CO_2 level. $D_{CO_2(g)}$ is the diffusion rate (mol/m²/s), calibrated by fitting measured $CO_2(g)$ over depth, and A is the surface area (m²). Because diffusion rates are highest in top soil, $D_{CO_2(g)}$ was set the highest at the soil surface (2.5 × 10⁻⁴ mol/m²/s) and exponentially decreased to 2.5 × 10⁻⁹ mol/m²/s in the deep zone. In CrunchTope, this rate was set up in the form of the Transition State Theory rate law (Plummer et al., 1978). The approximation for diffusion here aims to capture the first-order dynamics with data constraints and to avoid overburdening the model with multiphase flow dynamics without relevant data. Similar approximations have been used in Heidari et al. (2017) and Wen et al. (2021).

The model does not include the rate dependence of carbon transformations on temperature and soil moisture; thus, the overall rates are similar across hydrological gradients. Although not ideal, this approach enables the differentiation of the effects of varying flow paths and permeability distribution on reactions and export fluxes without the confounding effects of temperature and soil moisture. In addition, variations in water table depth and flow paths reflect the wetness condition at the site.

3.3. Model Calibration

Reaction parameters in the model for shallow soil processes were calibrated with constraints from direct field observations. They include averaged soil pore water chemistry data (DOC, alkalinity, Ca, Si, and Na concentrations) and soil CO₂ (Pabich et al., 2001; Sullivan et al., 2019). Most parameters for deep subsurface processes were taken from literature (e.g., porosity and permeability, mineral percentage, and OC abundance), due to the lack of measurements at the site. The reaction parameters for deep subsurface processes were calibrated by comparing simulated water chemistry to literature values with similar lithology and land cover ("+" in Figure 4)

WEN ET AL. 6 of 26



Table 1
Key Reactions and Kinetic and Thermodynamic Parameters^a

Reaction	$\log_{10} K_{eq}^{ \mathbf{b}}$	$\log_{10} k$ $(\text{mol/m}^2/\text{s})^{c,d}$	Specific surface area (m²/g) ^d
Bio-mediated reactions: Root respiration + OC decomposition ^b			
$(1) OC(s) \rightarrow 500DOC$	-	$10^{-6.7}$	5.0
$(2) DOC \rightarrow 4.8CO_2(aq)$	-	$10^{-4.5}$	1.0
$(3) Roots \rightarrow CO_2(aq)$	-	-	-
CO ₂ partitioning in gas and water phases ^c			
$(4) \operatorname{CO}_2(g) \to \operatorname{CO}_2(g *)$	-3.40	$10^{-5.0}$	1.0
$(5) \operatorname{CO}_2(aq) \leftrightarrow \operatorname{CO}_2(g)$	-1.50	-	-
$(6) \operatorname{CO}_2(aq) + \operatorname{H}_2\operatorname{O} \leftrightarrow \operatorname{H}^+ + \operatorname{HCO}_3^-$	-6.35	-	-
$(7) HCO_3^- \leftrightarrow H^+ + CO_3^{2-}$	-10.33	-	-
Sorption		Soil sorption capacity	
$(8) \equiv X + DOC \leftrightarrow \equiv XDOC$	$10^{0.2}$	7.5×10^{-5}	mol/g soil
Chemical weathering ¹			
(9) $CaCO_3(s) + CO_2(aq) + H_2O \leftrightarrow Ca^{2+} + 2HCO_3^-$	-4.52	-6.69	0.84
$CaCO_3(s) \leftrightarrow Ca^{2+} + CO_3^{2-}$			
$CaCO_3(s) + 2H^+ \leftrightarrow Ca^{2+} + 2HCO_3^-$			
$(10) \text{Ca}_{0.613} \text{Na}_{0.387} \text{Al}_{1.613} \\ (\text{SiO}_4)_{2.387} \\ (s) + 6.452 \\ \text{H}^+ + 1.548 \\ \text{H}_2 \\ \text{O} \\ \leftrightarrow 0.613 \\ \text{Ca}^{2^+} + 1.613 \\ \text{Al}^{3^+} + 0.387 \\ \text{Na}^+ + 2.387 \\ \text{H}_4 \\ \text{SiO}_4 \\ (aq) \\ \text{Na}^{4^+} + 1.548 \\ $	18.11	-11.30	6.70×10^{-4}
$\text{Ca}_{0.613} \text{Na}_{0.387} \text{Al}_{1.613} \left(\text{SiO}_{4} \right)_{2.387} \left(s \right) + 8.000 \text{H}_{2} \text{O} \\ \leftrightarrow 0.613 \text{Ca}^{2+} + 1.613 \text{Al}^{3+} + 0.387 \text{Na}^{+} + 2.387 \text{H}_{4} \text{SiO}_{4} \left(aq \right) + 6.452 \text{OH}^{-} \\ + 0.387 \text{Na}^{-} + 2.387 \text{H}_{4} \text{SiO}_{4} \left(aq \right) + 6.452 \text{OH}^{-} \\ + 0.387 \text{Na}^{-} + 2.387 \text{H}_{4} \text{SiO}_{4} \left(aq \right) + 6.452 \text{OH}^{-} \\ + 0.387 \text{Na}^{-} + 2.387 $			
(11) $Al_2Si_2O_5(OH)_4(s) + 6H^+ \leftrightarrow 2Al^{3+} + 2H_4SiO_4(aq) + H_2O$	6.81	-12.97	17.50

^aDetailed descriptions about rate laws were included in Text S2 in Supporting Information S1. All parameters refer to the condition at 15°C. ^bThe molecular formula of OC and DOC is assumed to follow the general form of $(C_6H_{12}O_6)_{1000}(s)$ and $C_{12}H_{24}O_{12}(aq)$, respectively (Riley et al., 2014). ^cThe rate constant k in the microbe mediated reactions 1 and 2 refers to μ in Equations S1–S2 in Supporting Information S1 (mol C/m²/s and mol C/mol biomass/s), respectively; For the local CO₂ production from roots (Reaction 3), with no explicit rate law, k is not defined and its local rate is directly assumed to be the same with that from OC (Equation S4 in Supporting Information S1). That is, root respiration was assumed to contribute 50% of the total soil respiration at the annual scale, which is within the reported range of 40%–60% in forest ecosystems (Hanson et al., 2000; Subke et al., 2006). ^dValues of K_{eq} were interpolated using the EQ3/6 database (Wolery et al., 1990), except Reactions 4–5, and Reaction 8 (i.e., $K_{eq,4}$, $K_{eq,5}$, and $K_{eq,8}$). $K_{eq,4}$ is used to represent the atmospheric CO₂ level; $K_{eq,5}$ is equal to the coefficient K_H in the Henry's law for CO₂. The value for $K_{eq,8}$ and the soil sorption capacity was from Oren and Chefetz (2012) and Jin et al. (2010), respectively. ^eReaction 4 approximates the process of the gas CO₂ diffusing into atmosphere by having a solid phase "CO₂(g*)" that acts as an atmospheric sink that can infinitely take in the released CO₂(g). ^fThe kinetic rate parameters and specific surface areas for mineral dissolution and precipitation (Reactions 9–11) were from Palandri and Kharaka (2004).

(McElwee et al., 1995; Pabich et al., 2001; Whittemore et al., 2014). As summarized in Table 2, this encapsulates our best efforts to constrain the model based on our knowledge of the Fitch site. One limitation is the lack of time-resolved water chemistry data, which limits the extent to which the model can capture the dynamics.

The model performance was evaluated using the Nash-Sutcliffe efficiency (NSE) that quantified the residual variance of model outputs compared to measurements (Moriasi et al., 2007). To reproduce soil CO_2 and pore water chemistry data to the satisfactory NSE level (>0.5), we first set the rate constant of OC decomposition (μ_{OC}) using literature values (Ahrens et al., 2015; Wang et al., 2015) and then adjusted CO_2 production rates ($\mu_{CO_2,OC}$) based on the reported ranges for forests (Carey et al., 2016). Lastly, we calibrated the $CO_2(g)$ diffusion rate ($D_{CO_2(g)}$) with reported soil CO_2 fluxes from 10^{-5} – 10^{-6} mol C/m²/s (Heinemeyer et al., 2007) at the soil surface to 10^{-9} mol C/m²/s in deep layers. All these calibrations ultimately lead to the reproduction of the depth profiles of measured soil CO_2 , alkalinity, Ca, Ca, and Ca and Ca and Ca and Ca are reported to the reproduction of the depth profiles of measured soil CO_2 , alkalinity, Ca, Ca, and Ca and Ca are reported to the reproduction of the depth profiles of measured soil CO_2 , alkalinity, Ca, Ca, and Ca are reported to the reproduction of the depth profiles of measured soil CO_2 , alkalinity, Ca, Ca, and Ca are reported to the reproduction of the depth profiles of measured soil CO_2 .

WEN ET AL. 7 of 26

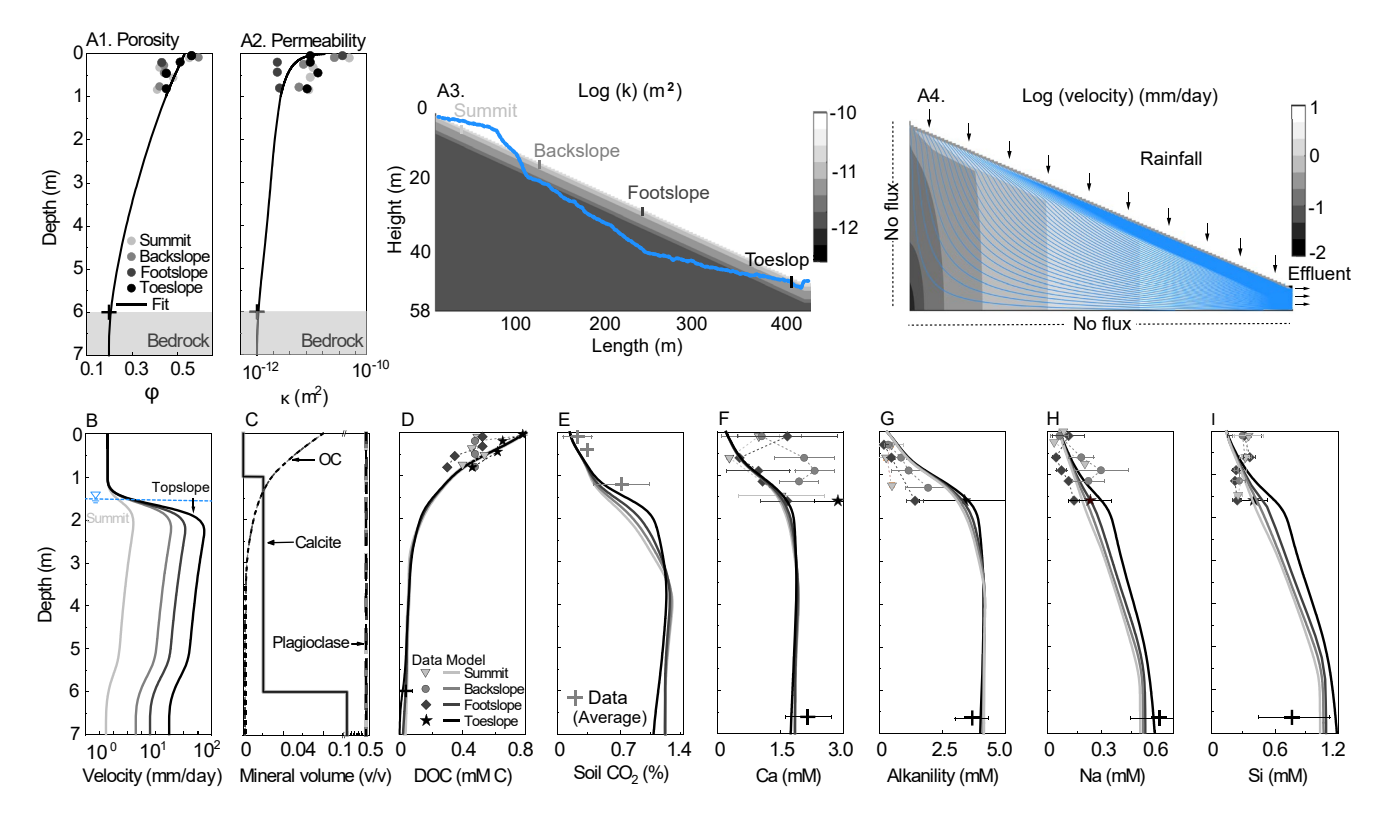


Figure 4. Top row: (a1) Depth profiles of porosity (field measurements), (a2) depth profile of permeability, estimated from Kozeny-Carman equation, (a3) hillslope permeability distribution, (a4) simulated flow velocity distribution. Blue lines in (a4) are flow paths. Areas with more blue lines indicate converging flow paths and therefore higher flow velocities. Bottom row: (b) Depth profiles of flow velocities, (c) mineral volume fraction (v/v), (d) DOC (mM C), (e) soil CO₂ (%), (f) Ca, (g) alkalinity, (h) Na, and (i) Si. Units of all solute concentrations are mM. Symbols are the average of field data; error bars are for one standard deviation; solid lines are model outputs. The dash line in (b) represents the prescribed water table depth (WTD) in the model based on field data. Overall, the top 6 m of the subsurface contributed >91% of stream water and was the most hydrologically active.

3.4. Numerical Experiments

To differentiate the impacts of hydrological conditions and subsurface physical structures, we designed numerical experiments with different flow regimes and shallow-versus-deep permeability contrasts while using the same reaction parameters and conditions as the base case at Fitch (e.g., organic carbon content, and mineralogy).

3.4.1. Subsurface Physical Structures

Three shallow-versus-deep permeability contrast scenarios were set up with different b values in $\kappa = \kappa_0 z^{b_\kappa}$ for the layers above the bedrock (<6 m). The scenario without a shallow-versus-deep permeability constrast, named LContrast (for Low contrast), has a b_κ value of 0, such that permeability is homogeneous over depth. The scenario with median shallow-versus-deep constrast (MContrast for medium) has a b_κ value of -0.4, the same set up as the base case at Fitch. The high constrast case (HContrast for High) has a b_κ value of -2.0 and a steep permeability decline over depth. The value of κ_0 are the same 1.7×10^{-11} m² in all three cases. The permeability of the parent rock (below 6.0 m) was kept constant at 1.7×10^{-11} m², 1.0×10^{-12} m², and 7.8×10^{-14} m² in LContrast, MContrast, and HContrast, respectively, based on typical ranges in literature (Elhakim, 2016). All other parameters (e.g., hillslope topography, reaction rate parameters, OC and mineral content) are the same in all three cases. The hillslope model was set up with no flow at the left and bottom boundaries such that all water entering the hill eventually leaves the hill via the toeslope (Figure 4a4).

3.4.2. Rising and Falling Water Tables Across Hydrological Gradients

This work focused on changing hydrological conditions and set the temperature at 15°C in all simulation cases. Field observations (Figure S1 in Supporting Information S1) indicate different water table depths at different rain-

WEN ET AL. 8 of 26



Table 2	
Main Model Input Parameters and Corresponding Data	Constraints

	Parameters	Source for constrain	Description
Domain	Size (length, height, slope)	Fitch observation	Section 3.1
Physical properties	Porosity	Fitch observation	Section 3.1
	Permeability		
Hydrological conditions	Discharge	Fitch observation	Section 3.1
	Water table depth (WTD)		
	Water saturation		
Subsurface chemical properties	Rainwater (injecting)	Fitch observation	Sections 2
	CO ₂ (initial)		& 3.1
	Subsurface water chemistry (initial)		
	OC and root abundance		
	Mineralogy abundance		
	OC decomposition rate constant μ_{OC}	Fitch observation: soil CO ₂ and water chemistry	Sections 2,
	CO_2 production rate constant $\mu_{CO_2,OC}$		3.2 and S2
	$CO_2(g)$ diffusion rate $D_{CO_2(g)}$		32
	Chemical weathering, including kinetic rate constant, equilibrium constant, and mineral surface area	Literature-derived (Jin et al., 2010; Oren & Chefetz, 2012; Palandri & Kharaka, 2004; Wolery et al., 1990)	Sections 3.2 and S2

fall events, from 2.5 m at 0.08 mm/day (very dry) to 0.5 m at 8.0 mm/day (very wet). We therefore prescribed the unsaturated–saturated interface to be from 2.5 to 0.5 m in the model, depending on the corresponding discharge conditions. Five hydrological conditions were run in each permeability contrast scenario, yielding to a total of 15 cases. Each case was run until steady state, when concentrations at the domain outlet became relatively constant with time (within \pm 5%).

3.5. Water Transit Time, Concentrations, Rates, and Fluxes at the Hillslope Scale

3.5.1. Water Transit Time

We used a "smart" tracer that goes through the decay process following zero-order kinetics $\frac{dC}{dt} = -k_{decay}$, where k_{decay} is the decay rate (=10⁻⁴ mol/L/a). The transit time (τ_i) of water arriving at a grid cell i can be estimated through the local tracer concentration following the solution of the equation $\tau_i = t - 0 = \frac{C_0 - C_i}{k_{decay}}$, where C_0 and C_i are the tracer concentration in the rainfall and pore water in the grid cell i at time t. The tracer was simulated with a concentration in the rainfall (C_0) of 0.9 mol/L and an initial zero concentration. The mean transit times in stream (τ_{stream}), shallow soil (τ_{sw}), and deep groundwater (τ_{gw}) were calculated using mean concentrations (averaged over depth) coming out of the soil zone (upper 3.0 m), groundwater zone (below 3.0 m), and stream using $\tau_{sw} = \frac{C_0 - C_{sw}}{k_{decay}}$, $\tau_{gw} = \frac{C_0 - C_{GW}}{k_{decay}}$, and $\tau_{stream} = \frac{C_0 - C_{stream}}{k_{decay}}$, respectively.

3.5.2. Solute Concentrations in Soil Water, Deep Groundwater, and Stream

We define the top 3.0 m as the shallow soil water zone (SW); the water below 3.0 m was considered as the deeper GW. Mean solute concentrations in SW (C_{SW}) were calculated as $\frac{\sum (C_{i,SW} \times u_i)}{\sum u_i}$, where u_i is flow velocity and $C_{i,SW}$ is the solute concentration in grid block i in soil zone (10 grid blocks away from the toeslope outlet to avoid mixing effects at the outlet). Similarly, mean solute concentrations in GW (C_{GW}) were calculated as $\frac{\sum (C_{i,GW} \times u_i)}{\sum u_i}$, where $C_{i,GW}$ is the local concentration in the grid block i of the GW zone close to the hillslope outlet. The stream concentration C_{stream} is the average effluent concentration at the hillslope outlet, calculated as $\frac{\sum (C_i \times u_i)}{\sum u_i}$ with the solute concentration C_i and flow velocity u_i in the grid block i at the effluent. We also tested 2.0 and 4.0 m as soil depths. The calculated mean soil water and groundwater chemistry varied but the trend remained the same.

WEN ET AL. 9 of 26



3.5.3. Hillslope Reaction Rates

Reaction rates R at the hillslope scale are the sum of the local rates in individual grids (r_i) multiplied by the corresponding water volume in each grid (V_i) . The rate of net DOC production is $R_{\text{DOC}} = \sum (r_{i,\text{DOC}} \times V_i)$, where $r_{i,\text{DOC}}$ is the difference between OC decomposition and DOC mineralization rates (Reactions 1–2, Equation S3 in Supporting Information S1). The net CO_2 production rate is $R_{\text{CO}_2} = \sum \left(r_{i,\text{CO}_2} \times V_i\right)$, where r_{i,CO_2} includes both DOC decomposition (Reaction 2) and root respiration (Reaction 3) in the grid i (Equation S4 in Supporting Information S1). Mineral weathering rates are $R_{\text{cal}} = \sum (r_{i,\text{cal}} \times V_i)$ and $R_{\text{plg}} = \sum \left(r_{i,\text{plg}} \times V_i\right)$. They follow the transition-state theory rate law (Equation S6 and Equation S7 in Supporting Information S1, respectively). The overall carbon production rate (R_{C}) from OC and roots equals the sum of R_{DOC} and R_{CO2} (Figure 2).

3.5.4. Biogeochemical Export Fluxes

The export fluxes F (Figure 2) include the vertical upward flux of CO_2 to the atmosphere ($F_{CO_2,V,up}$) and the lateral fluxes of dissolved organic and inorganic carbon into the stream ($F_{DOC,L}$ and $F_{DIC,L}$). The vertical flux $(F_{\text{CO}_2,V,up})$ is the sum of local CO_2 diffusion rates $r_{i,D,\text{CO}_2(g)}$ (Equation S5 in Supporting Information S1) across the entire hillslope (i.e., $F_{\text{CO}_2,V,up} = \sum r_{i,D,\text{CO}_2(g)}$). Normally, only the top soil layer releases CO₂ to the atmosphere and CO₂ in deeper depths transport CO₂ to the top layer. Gas transport however was not explicitly simulated in the model. The summation of gas diffusion in deeper grids, albeit with much lower upward diffusion rates, counts for CO₂ diffusion from depths to shallow soils that eventually emit CO₂ to the atmosphere. The lateral fluxes are the product of discharge (Q_T) and concentrations at the outlet grids. The lateral export of DOC (F_{DOCL}) is the summation of outlet lateral fluxes from the shallow soil $(F_{\text{DOC,L,SW}})$ and from deeper GW $(F_{\text{DOC,L,GW}})$. Similarly, $F_{\text{DIC,L}}$ is the summation of lateral SW fluxes ($F_{\text{DIC,L,SW}}$) and GW fluxes ($F_{\text{DIC,L,GW}}$). DIC came from both soil respiration and carbonate weathering. The soil respiration rates $(F_{\mathrm{DIC,SoilResp,L}})$ were estimated following $F_{\rm DIC,SoilResp,L} = F_{\rm DIC,L} - R_{\rm Cal}$. The overall carbon lateral export flux from biogenic carbon $F_{\rm C}$ was calculated as $F_{\rm C} = F_{\rm DIC, SoilResp, L} + F_{\rm DOC, L} + F_{{\rm CO}_2, V, up}$. The total carbon export flux from both soil respiration and carbonate weathering $(F_{\text{C,T}})$ is the sum of $F_{\text{DOC,L}}$, $F_{\text{DIC,L}}$, and $F_{\text{CO2,V,up}}$. The geogenic solute fluxes $(F_{\text{Ca,L}})$ and $F_{\text{Si,L}}$ were calculated as the production of discharge and concentrations of Ca and Si, respectively. For Si, F_{SiI} is the same as the overall silicate weathering rates (Reactions 10–11) at the hillslope scale. For Ca, $F_{\rm Ca,L}$ is the summation of calcite and silicate weathering rates multiplying corresponding stoichiometric coefficients.

4. Results

4.1. Effects of Hydrological Conditions

4.1.1. The Fitch Base Case (MContrast)

Simulated flow velocities (Figure 4a1-3) at Fitch varied laterally and decreased with depth (Figure 4a4). At 0.8 mm/day (0.3 m/a), the infiltrated water propagated vertically until reaching the shallow water table at 1.5 m and then flowed laterally into the stream (Figure 4b). The toeslope "collected" water from the entire hillslope such that flow velocities were much higher (~80.0 mm/day) than those at the summit (~2.4 mm/day). The depth profile of DOC almost overlapped at the four sampling locations (Figure 4d). They decreased with depth from ~0.8 to <0.1 mM C, consistent with common observations of higher carbon concentrations in shallow soils (Pabich et al., 2001; Sullivan et al., 2019). Soil CO₂, Ca, alkalinity, Na, and Si concentrations generally increased with depth in the upper 2.0 m of soil (Figures 4e-4i). The model captured these variations in shallow soils (NSE > 0.5), indicating the model includes key processes that control soil water chemistry patterns. Concentrations below 2.0 m were not measured but the simulated concentrations were consistent with literature values for Kansas (Macpherson, 2009; McElwee et al., 1995; Pabich et al., 2001; Whittemore et al., 2014). Soil CO_2 increased from 0.2% to ~1.3%, much higher than 0.04% in the atmosphere. Soil CO_2 concentrations were similar in the upper 1.5 m in all hillslope positions. The depth profiles of Ca and alkalinity mirrored those of soil CO₂, indicating soil CO₂ drove the concentration levels of these solutes. Although not included in the model, sulfate concentration increased from ~0.05 mM at 0.3 m to ~0.38 mM at 0.9 m, at least a half-order of magnitude lower than Ca and alkalinity concentrations at the same depth, indicating that carbonic acid is the major acid for mineral weathering. The dissolution of plagioclase elevated Na and Si concentrations both vertically (from soil to parent rock) and horizontally (from summit to toeslope).

WEN ET AL. 10 of 26



Several parameters tuned during the model calibration were important in reproducing data. They include rate constants of OC decomposition (μ_{CC} in Equation S1 in Supporting Information S1) that generated DOC, and rate constants of CO₂ production ($\mu_{\text{CO}_2,\text{OC}}$ in Equation S2 in Supporting Information S1). The depth profiles of soil CO₂ data were essential to capture the depth profiles of alkalinity and Ca data. In addition, $D_{\text{CO}_2(g)}$, a proxy for rates of CO₂ diffusion out of the domain (Equation S5 in Supporting Information S1), was important as it controlled the upward export of CO₂ into the atmosphere ($F_{\text{CO}_2,V,up}$). Mineral compositions of calcite and plagioclase were critical in reproducing Ca, Na, and Si concentrations. The soil water had abundant Ca, Na, and Si (Figure S2), suggesting a plagioclase formula of Ca_{0.61}Na_{0.39}Al_{1.61} (SiO₄)_{2.39} (s) (i.e., An60) and the dominant control of carbonate mineral. Other forms of plagioclase (e.g., An40 and 80) were tested but cannot reproduce Na and Si data.

4.1.2. Biogeochemical Spatial Profiles

Most reactions occurred in the upper 7.0 m of the subsurface and are therefore shown in Figure 5. Flow velocities generally peaked at the unsaturated–saturated interface (Figure 5a). As conditions became wetter, the water table was set to be increasingly shallower. Across different hydrological conditions, DOC production rates r_{DOC} were highest ($\sim 10^{-7}$ mol/m³/s) in the topsoil with abundant OC (Figures 5b and 4c) and lowest ($\sim 10^{-11}$ mol/m³/s) at 7.0 m. This pattern generally led to higher DOC and sorbed DOC in shallow soils. At 8.0 mm/day, high flow flushed more DOC into the stream and deeper subsurface, leading to higher sorbed DOC at depth (Figure 5d). Similarly, soil CO₂ production rates r_{CO_2} peaked in shallow soils and decreased with depth (Figure 5e). Topsoil CO₂ however was the lowest because of the highest vertical upward fluxes to the atmosphere (Figures 5f and 5g). The CO₂ production rates were not influenced as much by flow conditions, but CO₂ concentrations depended on flow conditions because of the flow influence on export. Under dry conditions, diffusion exported soil CO₂ upward but lateral export of DIC was slow such that soil CO₂ levels remained high (Cueva et al., 2019; Olshansky et al., 2019); under wet conditions, concentrations were lower because of rapid water flow and higher DIC lateral export (Figures 5f and 5g).

The pH generally increased with discharge whereas concentrations of Ca and DIC concentrations decreased with discharge (Figures 5h and 5i). At 0.08 mm/day, high soil CO_2 level and carbonate precipitation lowered pH (\sim 6.5). At 8.0 mm/day, fast flow led to rapid lateral export of soil CO_2 and carbonate dissolution, such that pH was much higher (\sim 8.0). Calcite dissolution rates peaked at the calcite—no calcite interface when calcite was in contact with relatively young water still at disequilibrium (Figure 5j). Calcite precipitated in the deep subsurface as Ca and carbonate built up and approached equilibrium. The dissolving—precipitating interface (black vs. white color) progressively deepened from \sim 2.0 m at 0.08 mm/day to \sim 6.5 m at 8.0 mm/day, as the faster flow also replenished the deeper subsurface rapidly with water at disequilibrium (Figure 5j). Plagioclase weathering was much slower than carbonate weathering and depended on pH. With pH increasing from low to high discharge, plagioclase dissolution rates decreased (Figures 5k and 5l).

4.1.3. Solute Concentrations in Different Waters

Soil and groundwater solute concentrations varied with discharge. For DOC, both soil and groundwater concentrations increased with discharge; Soil water concentrations ($C_{\rm SW}$) were higher than groundwater concentrations ($C_{\rm GW}$) (Figure 6a). The $C_{\rm SW}$ versus $C_{\rm GW}$ difference was small under dry conditions and increased under wet conditions, due to the flushing of DOC via top soils with more abundant DOC. Conversely, the $C_{\rm SW}$ and $C_{\rm GW}$ difference of other solutes (${\rm CO_2}$, H⁺, DIC, Ca, and Si) was generally higher under dry conditions and lower under wet conditions (Figures 6b–6f). The elevated water tables at high flow enhanced flow mixing at the toeslope and led to similar $C_{\rm SW}$ and $C_{\rm GW}$ before they entered the stream.

Stream water was a mixture of soil water and groundwater. Under wet conditions, soil water dominated stream water; under dry conditions, groundwater dominated streamflow. The stream concentration therefore approximated $C_{\rm GW}$ under dry conditions and mirrored $C_{\rm SW}$ under wet conditions. Stream DOC concentrations increased as discharge increased (flushing pattern, Figure 6a). Stream DIC, Ca, and Si concentrations decreased with increasing discharge, exhibiting a dilution pattern (Figures 6d–6f). Stream ${\rm CO_2}({\rm aq})$ decreased from 6.8 to 0.04 mM, as stream pH increased and DIC decreased from dry to wet conditions. Generally, ${\rm CO_2}({\rm aq})$ reached the highest level at the highest DIC and lowest pH.

WEN ET AL. 11 of 26



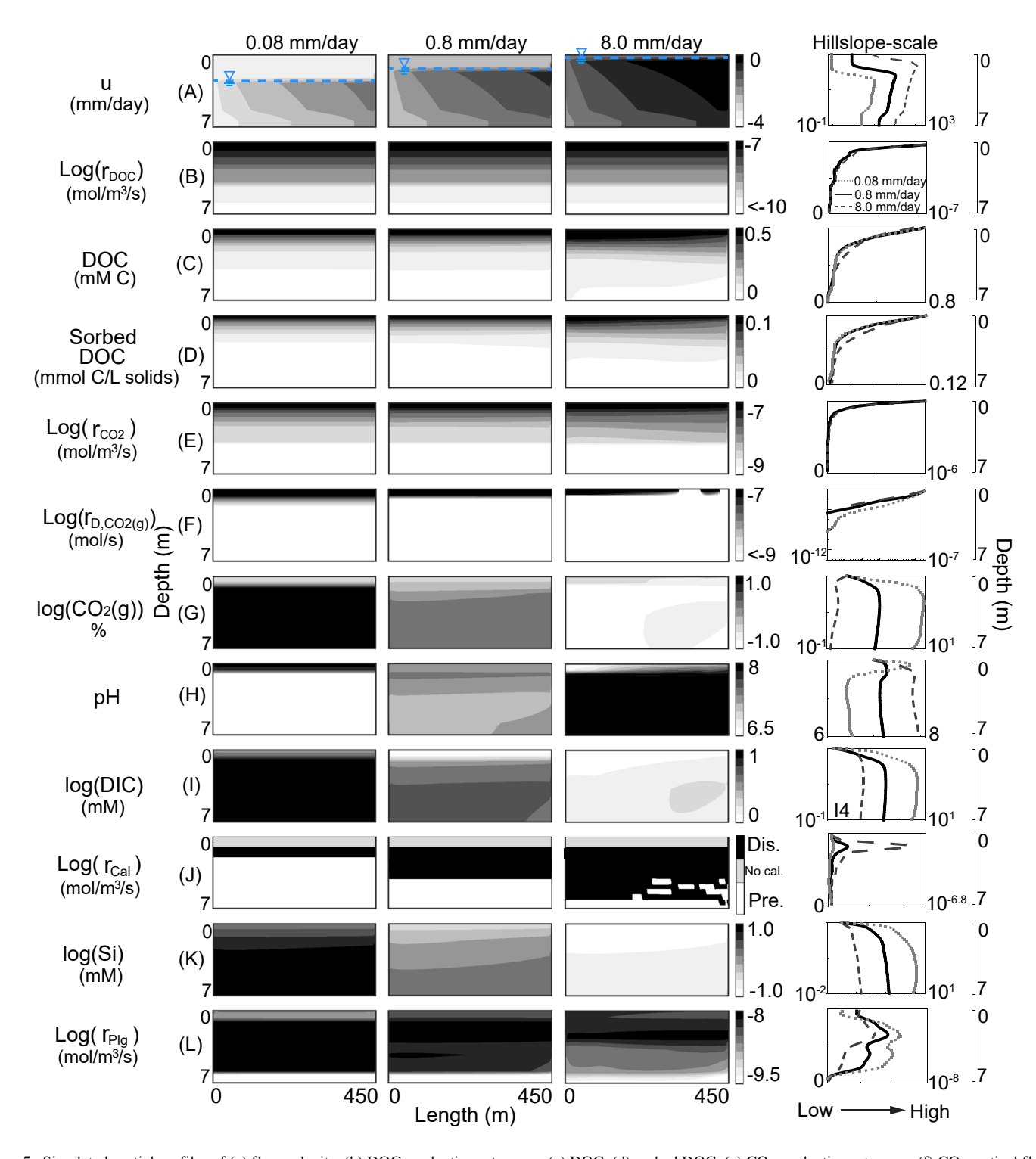


Figure 5. Simulated spatial profiles of (a) flow velocity, (b) DOC production rate, r_{DOC} , (c) DOC, (d) sorbed DOC, (e) CO₂ production rate, r_{CO_2} , (f) CO₂ vertical flux, (g) soil CO₂(g) (%), (h) pH, (i) DIC, (j) carbonate weathering (calcite) rate, r_{cal} , (k) Si, and (L) silicate weathering (plagioclase) rate, r_{plg} at discharge of 0.08, 0.8, and 8.0 mm/day. All figures are for the top 7 m from the ground surface. The hillslope outlet is at the right. The right column shows horizontally-averaged quantities over depth at 0.08 mm/day (dotted), 0.8 mm/day (black), and 8.0 mm/day (dashed), respectively. The blue dash line in (a) is the prescribed unsaturated–saturated interface in the model following WTD data at Fitch. Soil CO₂(g) (%) was calculated using Henry's law based on CO₂(aq) and Henry's law constant.

WEN ET AL. 12 of 26

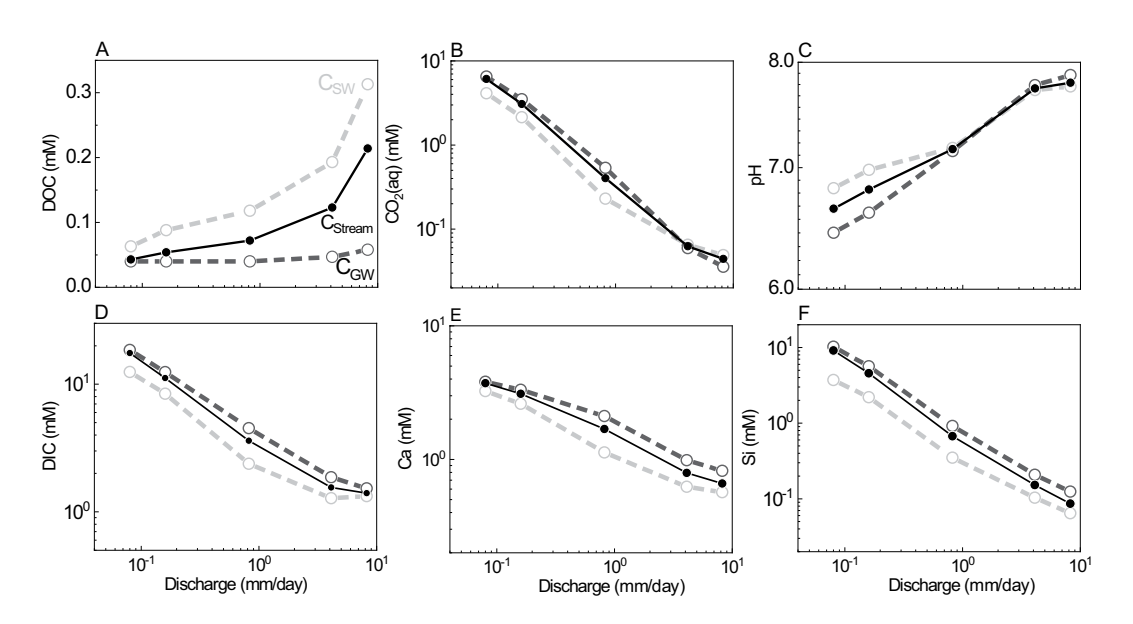


Figure 6. Simulated soil water (C_{sw} ; gray dash) and groundwater (C_{GW} ; black dash) solute concentrations (at the toeslope before entering the stream) as a function of discharge (X-axis): (a) DOC, (b) CO₂(aq), (c) pH, (d) DIC, (e) Ca, and (f) Si. Stream DOC (C_{stream} , solid black line) exhibited a flushing pattern (increasing concentration with discharge) whereas the inorganic carbon (CO₂ and DIC), Ca, and Si showed a dilution pattern (decreasing concentration with discharge). These solutes also have higher groundwater concentrations compared to soil water, the opposite of DOC.

4.1.4. Carbon Rates and Fluxes at the Hillslope Scale

The rates of net DOC production (i.e., $R_{\rm DOC} = R_{\rm CO_2,OC} = F_{\rm DOC,L}$) increased from ~1.0 to 284 mol C/a (from <0.1% to 12% of the total processed carbon) when discharge increased from 0.08 to 8.0 mm/day (Figure 7), because higher discharge flushed DOC out quickly and lessened the mineralization of DOC to DIC and/or CO₂ ($R_{\rm CO_2,OC}$). For the same reason, the rates of soil respiration or the net CO₂ production ($R_{\rm CO_2} = R_{\rm CO_2,rt} + R_{\rm CO_2,OC}$) decreased from ~2,412 to 2,152 mol C/a with increasing discharge. The rates of $R_{\rm CO_2}$ are generally more than an order of magnitude higher than $R_{\rm DOC}$. In addition, more inorganic carbon was produced under dry conditions compared to wet conditions. The hillslope carbon transformation rate ($R_{\rm C}$) from OC and roots, which is the sum

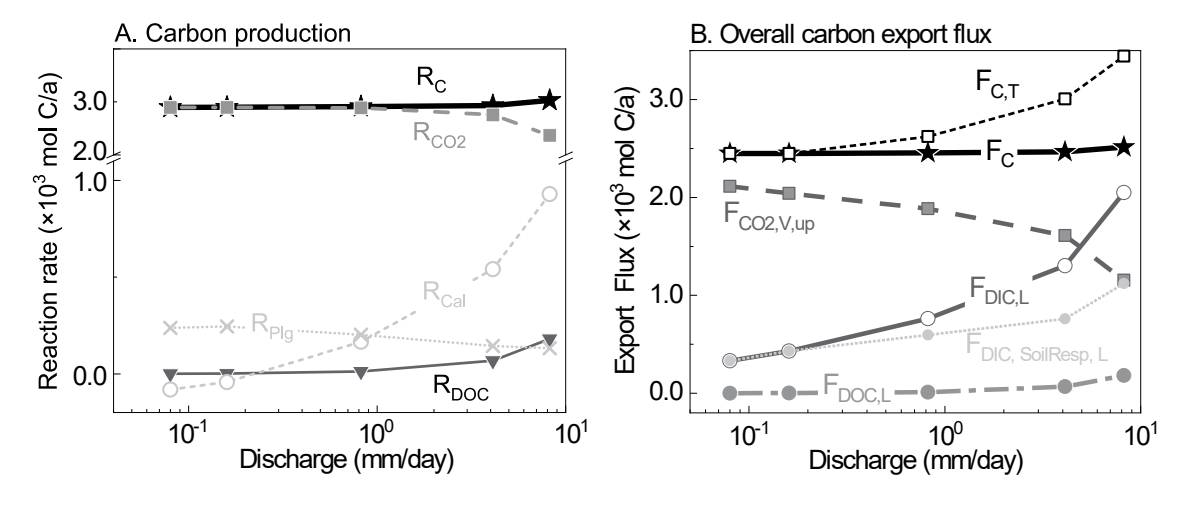


Figure 7. (a) Hillslope-scale soil respiration rates ($R_{\rm C}$), production rates of DOC and CO₂ ($R_{\rm DOC}$, $R_{\rm CO_2}$), and calcite and plagioclase weathering rates ($R_{\rm cal}$ and $R_{\rm plg}$); (b) DOC and DIC export fluxes. $F_{\rm DIC,L}$ is the total lateral DIC flux; $F_{\rm DIC,SoilResp,L}$ is the flux of carbon originated from soil respiration, excluding those from carbonate dissolution. Dry conditions favored the production and vertical fluxes of CO₂ and calcite precipitation; Wet conditions enhanced the production of DOC, lateral export of DIC (especially via shallow soil water), and calcite dissolution (also see Figure S3 in Supporting information S1 for Ca and Si export fluxes, and Tables S2 and S3 in Supporting information S1 for reaction and export rates of MContrast case under different discharge conditions).

WEN ET AL. 13 of 26



of $R_{\rm DOC}$ and $R_{\rm CO_2}$, increased with discharge slightly but remained close to ~2,400 mol C/a under different hydrological conditions.

Calcite weathering rates increased considerably from -80 mol/a (precipitation) at 0.08 mm/day to $\sim 916 \text{ mol/a}$ (dissolution) at 8.0 mm/day. This is expected as calcite dissolves quickly and depends on rapid water flow to maintain disequilibrium. The plagioclase weathering rates did not vary as much with discharge, because plagioclase dissolves slowly (Reaction 10 in Table 1) and is typically at disequilibrium. In addition, plagioclase weathering depended on pH, which increased with discharge and offset the enhanced dissolution rates from rapid flow. In summary, dry conditions produced more DIC, less DOC, and precipitated carbonate; wet conditions produced less DIC, more DOC, and dissolved carbonate.

As soil respiration remained similar, the fluxes of carbon from soil respiration, $F_{\rm C}(=F_{\rm CO_2,V,up}+F_{\rm DIC,SoilResp,L}+F_{\rm DOC,L})$, also remained similar across hydrological gradients. Total carbon fluxes ($F_{\rm C,T}=F_{\rm CO_2,V,up}+F_{\rm DIC,L}+F_{\rm DOC,L}$), the carbon from both soil respiration and carbonate weathering, however, increased with flow (Figure 7b) due to the higher rates of carbonate weathering at high flow that contributed more geogenic carbon. At 0.08 mm/day, the vertical upward CO₂ flux was 2,084 mol C/a (~86%); DOC ($F_{\rm DOC,L}=F_{\rm DOC,L,SW}+F_{\rm DOC,L,GW}$) and DIC ($F_{\rm DIC,L}=F_{\rm DIC,L,SW}+F_{\rm DIC,L,GW}$) exported laterally at ~1.0 mol C/a and ~259 mol C/a, respectively. Almost all lateral DIC fluxes were from soil respiration and via deeper groundwater flow paths (83%, or 214 mol C/a, Figure S3 in Supporting Information S1). The lateral DOC flux was close to zero ($F_{\rm DOC,L,SW}$, Figure 7b).

At 8.0 mm/day, CO_2 vertical fluxes, $F_{CO_2,V,up}$, were 1,138 mol C/a. The lateral DOC fluxes increased to 284 mol C/a, 90% of which exported via SW due to much higher water fluxes and higher DOC concentrations in shallow soils. The overall DIC lateral flux was also much higher ($F_{DIC,L} = 2,019 \text{ mol C/a}$), with carbonate dissolution and soil respiration contributing ~916 mol C/a and ~1,103 mol C/a, respectively (Figure 7b). Although not shown here, cation fluxes (Ca and Si) generally followed similar trends as their weathering rates (R_{Cal} and R_{Plg} , Figure 7a and Figure S3 in Supporting Information S1). In summary, dry conditions exported more CO_2 vertically to the atmosphere but less DIC and DOC laterally; wet conditions exported less CO_2 vertically to the atmosphere but more laterally.

4.2. Effects of Shallow-Versus-Deep Permeability Contrast

4.2.1. Water Partitioning and Transit Times

The depth distribution of permeability determines the relative proportions of water fluxes from different depths. In HContrast, steep permeability decline (soil surface-bedrock permeability contrast of $\sim 10^2$) resulted in about 48% of total water fluxes to discharge from the upper 3.0 m of subsurface (Figure 8a2–b2). In contrast, about 15% of total water fluxes came out of the upper 3.0 m in LContrast (homogeneous) (Figure 8a1–b1). The corresponding values for the upper 6.0 m were 96% and 65% in HContrast and LContrast, respectively.

The stream water is a mixture of soil water and groundwater from different depths. The depth profiles of shallow and deep flow entering the stream followed similar trends among cases with different permeability distribution (Figure 8c). At 0.8 mm/day, flow rates increased with depth before peaking at the shallow water table (\sim 1.5 m) and declined below that depth. The vertical contrasts in flow rates were highest in HContrast. The proportion of SW versus GW varied with discharge because of the rising and falling water table (Figure S4 in Supporting Information S1). This variation in water table depths led to different water partitioning between soil water and groundwater under different scenarios (Figure 8d). In MContrast, at $Q_{\rm T}=0.08$ mm/day, water table was deep and the deeper groundwater dominated, contributing to 83% of the stream flow ($Q_{\rm GW}/Q_{\rm T}=0.83$). At $Q_{\rm T}=8.0$ mm/day, deep groundwater contributed about 36% of the streamflow. The GW proportions to streamflow varied most in HContrast, decreasing from 0.73 to 0.14 from very dry to very wet conditions, compared to persistently high GW proportion (0.93–0.73) in LContrast. LContrast also had the youngest GW. The mean SW age varied from \sim 0.4 to 47 years, and the GW age varied from \sim 7.3 to 571 years. The stream water age ($\tau_{\rm stream}$) varied from \sim 5.2 to 531 years, generally younger under wet conditions (Figure 8e). Larger permeability contrast at different depths resulted in larger variations in GW age compared to SW.

WEN ET AL. 14 of 26

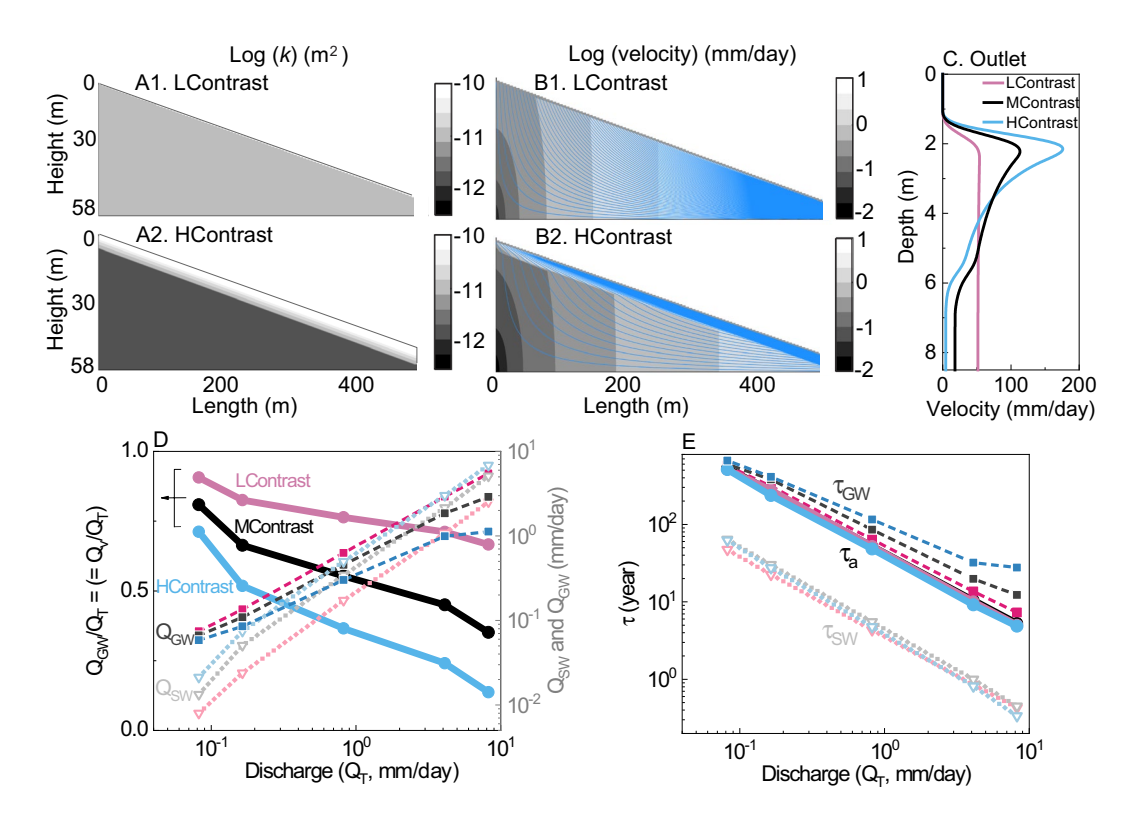


Figure 8. (a–b) Spatial profiles of permeability and flow velocities at a discharge of 0.8 mm/day in LContrast with homogeneous permeability distribution (top) and in HContrast with steep decline in permeability (bottom). The thin blue lines represent the flow lines. In LContrast, much more water flows through the deeper zone compared to HContrast. (c) Depth profiles of flow velocities at the hillslope outlet. (d) Flow rates of shallow soil water (Q_{SW} , dotted lines) and groundwater (Q_{GW} , dashed lines) that enters stream, and the corresponding relative contribution of groundwater to stream (Q_{GW}/Q_T , thick solid lines). (E) Mean transit time of stream water τ_{Stream} , soil water τ_{SW} , and groundwater τ_{GW} under different permeability contrast and discharge conditions. The GW proportion was generally highest in LContrast and lowest in HContrast, and decreased as discharge increased.

4.2.2. Biogeochemical Measures

The vertical profiles of geochemical variables were similar in different permeability contrast scenarios (Figure S5 in Supporting Information S1). Likewise, DOC and DIC concentrations were similar in different waters (SW, DW, and stream in Figures 9a and 9b) except under extreme wet conditions. Stream DOC concentrations were highest in HContrast because more water flows via the shallow organic-rich zone (Figure 9a). Stream concentrations of DIC, Ca, and Si were similar among all three cases (Figure 9b, Ca and Si are not shown here). The permeability contrast was more influential in determining lateral SW versus GW export fluxes. LContrast generally had the highest GW fluxes. For all solutes, GW fluxes were higher than SW fluxes under dry conditions (Figures 9c–9f). As the system became wetter, SW fluxes increased faster than GW fluxes such that they eventually dominated under wet conditions. HContrast had the most significant increase in SW fluxes, leading to the highest SW flux percentage, or lowest GW flux proportion under wet conditions.

Reaction rates and fluxes exhibited the largest differences across permeability contrast scenarios under extreme wet conditions (Figure S6 and Table S2 in Supporting Information S1). At 8.0 mm/day, $R_{\rm CO_2}$ in HContrast decreased from ~2,412 mol C/a at 0.08 mm/day to ~2,047 mol C/a at 8.0 mm/day. Correspondingly, $F_{\rm CO_2,V,up}$ was ~2,084 mol C/a at 0.08 mm/day and ~1,064 mol C/a at 8.0 mm/day. The vertical upward $\rm CO_2$ fluxes were highest in LContrast and lowest in HContrast. This is because HContrast has the highest SW that rapidly exported DOC and DIC out of the system, leaving less $\rm CO_2$ for vertical export. The difference among cases however was relatively small, about ~8% between extreme wet conditions. The differences in carbonate weathering rates across permeability contrast scenarios were also negligible except under very wet conditions (Figure S6 and Table S2 in Supporting Information S1). At 8.0 mm/day, HContrast had the fastest carbonate weathering rates

WEN ET AL. 15 of 26



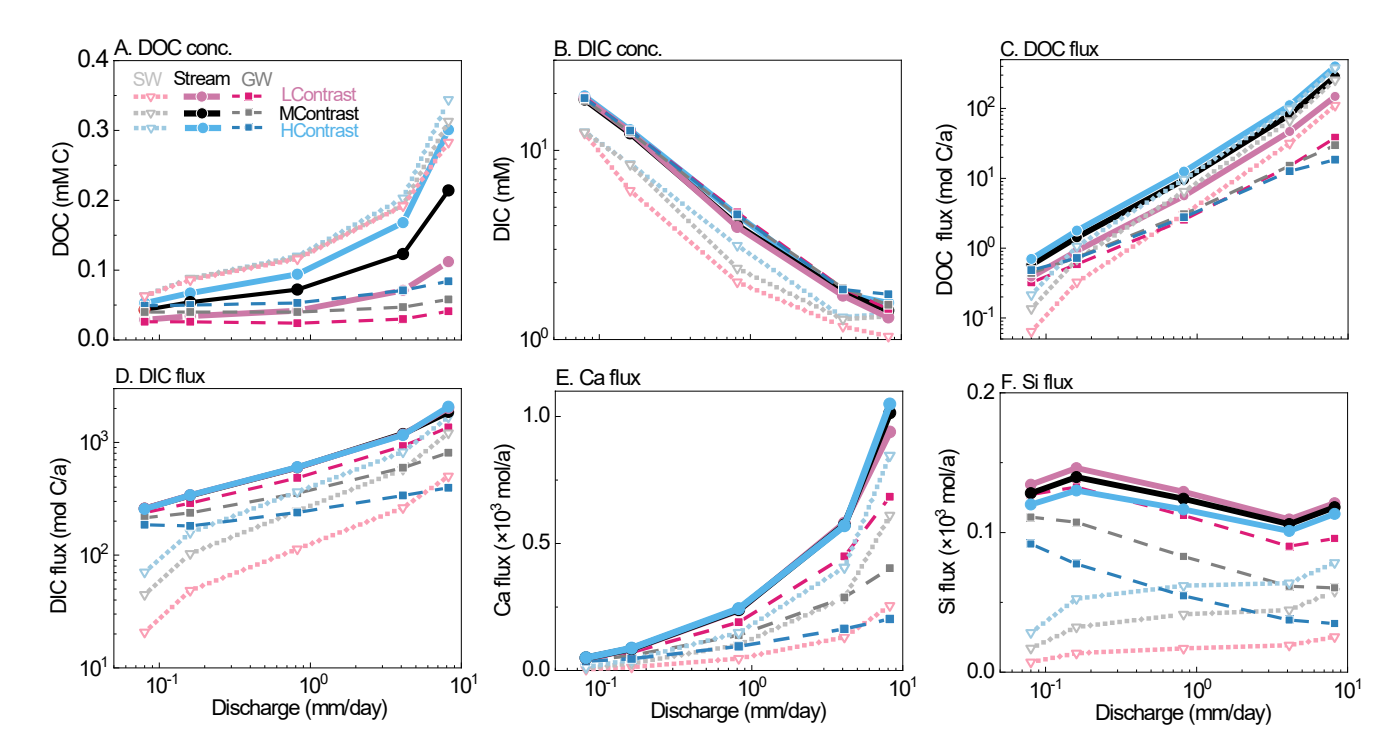


Figure 9. (a–b) Concentrations and (c–f) fluxes under different hydrological and permeability contrast conditions: (a) DOC, (b) DIC, (c) DOC fluxes, (d) DIC fluxes, (e) Ca fluxes, and (f) Si fluxes. Differences across permeability contrast scenarios were smaller than discharge-induced differences and were most pronounced under wet conditions. Higher permeability in shallow soil (HContrast) promoted solute lateral fluxes.

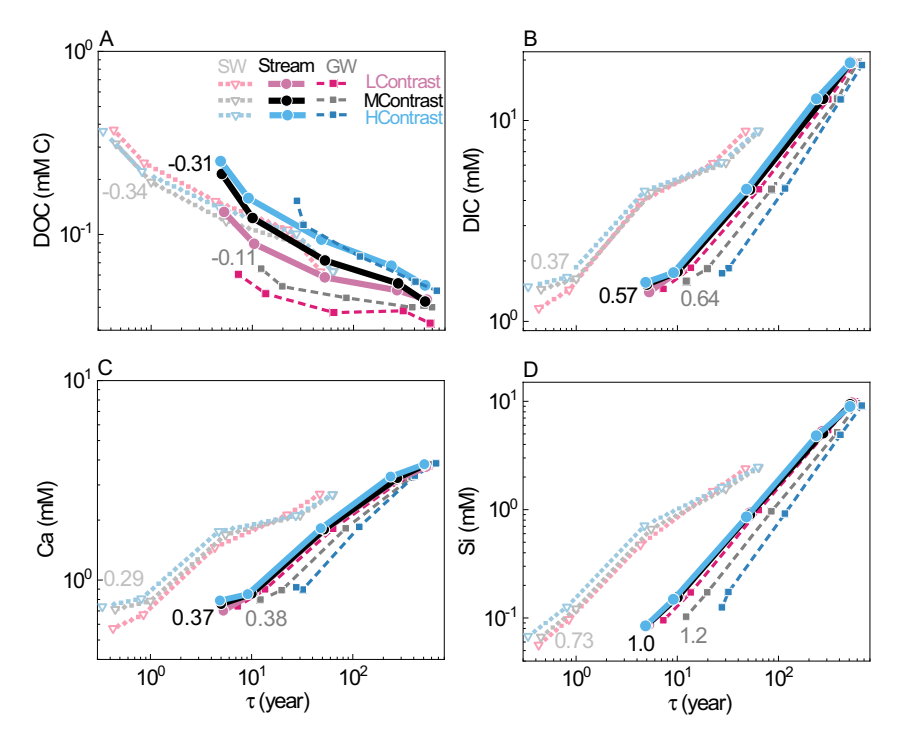


Figure 10. Concentrations versus water transit time: (a) DOC, (b) DIC, (c) Ca, and (d) Si. DOC concentrations were generally higher in younger waters. All other solutes had higher concentrations in older waters. The concentrations—transit time relationship approximated power law relationships (linear in loglog scale). The numbers are the average slopes of the C-t relationship ($C = a\tau^b$) in log-log scale.

WEN ET AL. 16 of 26

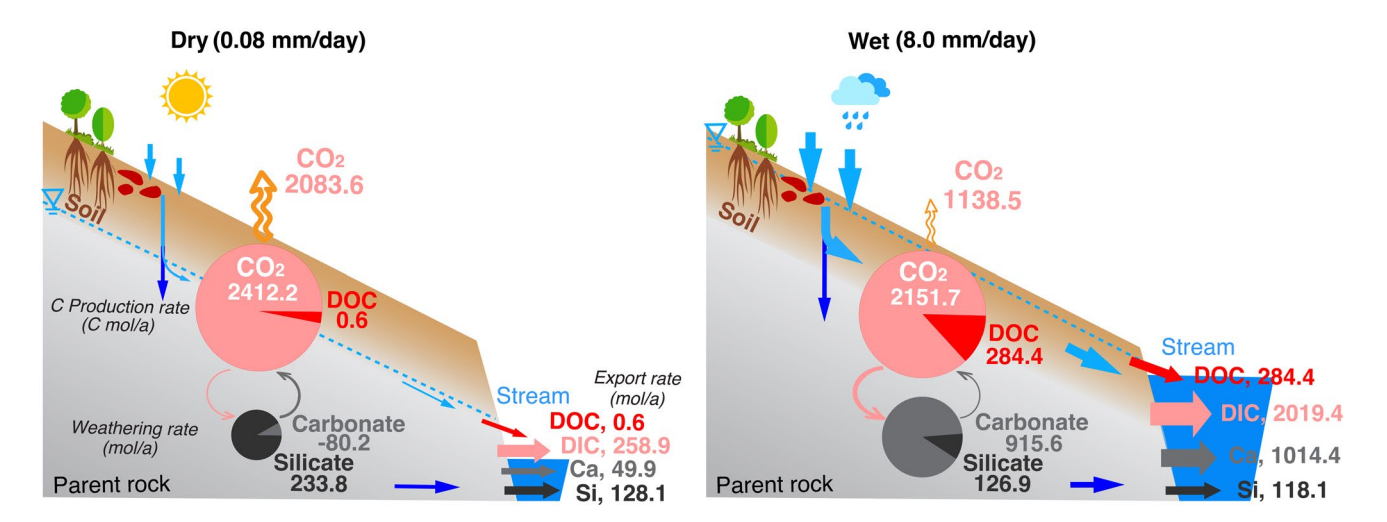


Figure 11. Quantification of rates and fluxes from hillslope RTM under dry and wet conditions. All carbon rates and fluxes are in units of C mol/a; all weathering rates are in units of mol/a. Droughts (0.08 mm/day, left) promoted upward emission of CO_2 gas, deeper flow paths, carbonate precipitation, and mineralization of organic carbon into inorganic carbon. Storms (8.0 mm/day) reduced CO_2 upward emission to the atmosphere and OC mineralization but promoted shallow flow paths, carbonate dissolution, DOC production, and lateral fluxes of IC intro streams.

 (R_{Cal}) , about ~10% higher than LContrast. The differences in silicate weathering rates in the three permeability contrast scenarios were less than 2%.

4.3. Concentration Dependence on Water Transit Time

The concentrations of all solutes strongly relate to water transit time, although the relationship differed for different solutes and different waters (Figure 10). DOC concentrations generally increased with decreasing water age, as younger water and higher water table carried more DOC in shallow soil. In contrast, DIC, Ca, and Si concentrations increased with water age, as weathering occurred to a large extent in the old water in deeper zones.

5. Discussion

This work examines (a) the rarely explored linkage among carbon transformation reactions, vertical and lateral carbon fluxes, and their intertwined connections with flow paths at the hillslope scale, and (b) the significance of hydrological extremes (e.g., from droughts to storms) and internal structure (vertical permeability contrast) in regulating reaction rates, fluxes, and stream chemistry. This work delineates an integrated "picture" for carbon cycling and terrestrial-aquatic connections demanded in literature (Keller, 2019; Tank et al., 2018). Existing terrestrial biosphere models account for vertical CO₂ transport but not lateral IC transport to streams and rivers, which ultimately evades to the atmosphere. Existing models therefore overestimate subsurface carbon storage and underestimate CO₂ emission (Butman et al., 2016). Results here indicate that the extent of errors may be more significant under wet conditions where higher proportions of terrestrial carbon are exported laterally in dissolved forms. The reactive transport model developed here can be considered as a basis for further studies constrained by time-resolved field data to explore terrestrial carbon cycling.

5.1. Connecting Carbon Transformation, and Vertical and Lateral Transport

Results here delineate an integrated framework that connects terrestrial carbon and cation production to solute export into streams (Figure 1 and Figure 11). Production of CO_2 in the top 1.0 m contributed >90% of total soil respiration. Carbon transformation rate (i.e., R_C in Figure 2) was ~5.6 mol C/m² (drainage area)/a at intermediate flow (0.8 mm/day), within the typical range of 2.0–50.0 mol C/m²/a reported for forest ecosystems under similar temperature conditions (Fang & Moncrieff, 2001; Raich & Schlesinger, 1992).

WEN ET AL. 17 of 26



The results underscore the predominance of hydrological conditions in controlling the relative magnitude of vertical and lateral carbon fluxes: droughts enhance carbon mineralization and vertical upward carbon fluxes back to the atmosphere, and storms and flooding promote lateral export of dissolved carbon into streams and rivers (Figure 11). Under dry (0.08 mm/day) and wet (8.0 mm/day) conditions, vertical carbon fluxes were about 86% and 51% of total soil respiration, respectively. Correspondingly, about 14% of inorganic carbon from soil respiration ($F_{\rm DIC,SoilResp,L}$) was laterally exported under dry conditions, compared to 49% under wet conditions (Figure 7b). This explains two observations: first, a considerable portion of DIC fluxes originates from soil respiration under dry conditions; second, riverine DIC fluxes from soil respiration positively correlates with discharge (Campeau et al., 2017; Zhong et al., 2017), and $\rm CO_2$ evasion from rivers can be substantial, especially in headwater streams (Hotchkiss et al., 2015; Raymond et al., 2013). The reactions and transport dynamics under dry and wet conditions resemble the dynamics under arid versus humid climates across United States (Li et al., 2022).

The projected DOC lateral fluxes can vary by two orders of magnitude (2×10^{-3} to 6×10^{-1} mol C/m²/a) across hydrological conditions, similar to the reported range of 6×10^{-3} mol C/m²/a (Mulholland, 1997) to 4×10^{-1} mol C/m²/a in temperate forests (Raymond & Saiers, 2010). The fluxes increase with discharge (Figure 7), echoing observations of elevated DOC export during storms potentially arising from enhanced connectivity and DOC desorption under wet conditions (Campeau et al., 2019; Piney et al., 2018). Results here however underscore two additional mechanisms: (a) less DOC may undergo transformation into inorganic carbon due to shorter water transit times under wet conditions (Figures 7a and 8e); and (b) high DOC fluxes can arise from rising water tables that flush out more DOC-enriched water in shallow soils (Figures 5c and 6a) (Barnes et al., 2018; Seibert et al., 2009; Zhi & Li, 2020; Zhi et al., 2019). Results here also support the observation that discharge, among many climate indexes, can be the single most important control on DOC fluxes (Worrall et al., 2004, 2008).

Soil respiration rates are often measured on the ground surface based on vertical fluxes (Bond-Lamberty & Thomson, 2010; Soper et al., 2017). Results here indicate that such measurements may underestimate respiration rates, because they do not count for the lateral transport of DIC. Similarly, because soil carbon storage is often inferred from vertical efflux from soil, not counting DIC lateral fluxes can overestimate terrestrial ecosystem carbon stocks (Liu et al., 2010). The extent of underestimation and overestimation may be particularly large under wet conditions, when the lateral DIC fluxes constitute about half of total produced IC.

The influence of permeability contrast and vertical connectivity on carbon transformation rates is generally higher under wet conditions, although its influence is overall small. This is because soil respiration mostly occurs in shallow soils: >90% of the total annual efflux occurs in the top meter of soil. The deeper subsurface generally has orders-of-magnitude lower carbon transformation rates than those in surface soils such that reaction rates at depth do not influence the overall rates as much (Figure 5 and S5 in Supporting Information S1). Permeability distribution, however, regulates flow partitioning and therefore the amount of dissolved carbon via deeper subsurface. Total DOC and DIC fluxes via the GW route maximized in LContrast (Figures 9c and 9d), whereas those via the SW route peaked in HContrast, as more DOC-enriched soil water flowed out of the shallow zone in HContrast.

5.2. Chemical Weathering at Hydrological Extremes

5.2.1. The Differential Dependence of Carbonate and Silicate Weathering Rates on Hydrological Conditions

Hydrological conditions influence carbonate and silicate weathering via different mechanisms. Carbonate weathering is fast and transport controlled such that it largely depends on water flow to drive the reaction to disequilibrium. The opposite is true for the slower silicate weathering (Reactions 9 and 10 in Table 1). Its rate is pH rather than flow dependent. Under dry conditions, the low flow rates and DIC export sustained soil CO_2 at higher levels and resulted in acidic soil water (pH \sim 6.5 at 0.08 mm/day) that accelerates silicate weathering.

Silicate weathering slowed down at high pH under wet conditions (pH = \sim 8.0 at 8.0 mm/day). The dependence of silicate weathering on CO₂ and pH has been well documented in theoretical and experimental work (Golubev et al., 2005; Penman et al., 2020; Winnick & Maher, 2018). Direct field observations addressing the relationship between soil CO₂, pH, and weathering rates under varied hydrological conditions are limited due to confounding environmental factors. Elevated soil pCO_2 at high temperature and low soil moisture have been observed to amplify silicate weathering (Andrews & Schlesinger, 2001). This work suggested that Si fluxes and silicate

WEN ET AL. 18 of 26



weathering rates were highest under dry conditions and decreased with discharge. Note that this may only hold true for the slow, kinetic-controlled weathering (i.e., transport time/reaction time <1). In tropical regions or during monsoons when transport time/reaction time >>1, silicate weathering rates might be directly proportional to precipitation or runoff (Tipper et al., 2006; West et al., 2005; White & Blum, 1995).

5.2.2. Carbonate Releasing or Storing CO₂?

The direction of the carbonate reaction $(CaCO_3(s) + CO_2(g) + H_2O \leftrightarrow Ca^{2+} + 2HCO_3^-)$, whether dissolution or precipitation, highly depends on hydrological conditions. When carbonate dissolves, it transforms soil CO_2 into DIC; when carbonate precipitates, it releases gaseous CO_2 . Model results here show that carbonate dissolved in shallow soils (1-2 m) when in direct contact with fresh rainwater (Figure 5j), but quickly reached equilibrium and precipitated with cations from plagioclase dissolution at higher pH and DIC in the deep subsurface (below 2 m). Under wet conditions, fast flow drove dissolution to rates as high as $\sim 900 \text{ mol/a}$, contributing more than a third of the overall inorganic carbon lateral fluxes (Figures 7a and 7b). Such calcite dissolution in shallow zones and precipitation at depth has been observed in calcite-dominated sites, especially when silicates provide extra cations (Monger et al., 2015; Wan et al., 2019; Zamanian et al., 2016). Pedogenic carbonate as soil inorganic carbon stocks is widely observed in arid and semi-arid regions (Stanbery et al., 2017; Zamanian et al., 2016). These results suggest that inorganic carbon can be stored under dry conditions as carbonate precipitates but can be released into water again during storms (Sagi et al., 2021).

These findings shed lights on the decade-long debate of whether soil carbonates and groundwater act as active carbon sinks or source (Ma et al., 2014; Sagi et al., 2021; Schlesinger, 1982; Schlesinger & Amundson, 2019; Schlesinger et al., 2009). Results here indicate that transition from droughts to storms can shift carbonate between a carbon sink and source via changing the carbonate reaction direction. Similar conclusions have been drawn in studies for Karst catchments (Liu et al., 2018; Zeng et al., 2019). In other words, soil carbonate can be both sources and sinks, depending on hydrologic regimes.

5.2.3. The Influence of Permeability Contrasts on Weathering Is Surprisingly Small

Contrasting the expectation that vertical connectivity is a dominant control on weathering deep in the subsurface (Xiao et al., 2021). Silicate weathering rates in LContrast and HContrast differed only by about 3%–7% under dry conditions. For carbonate weathering, its influence increased with discharge but still below 10% even under wet conditions, much smaller than the structure heterogeneity effects observed at the pedon scale (10s of centimeters) and meter scale (Wen & Li, 2018; Wen et al., 2021). At the pedon scale, the deeper flow facilitated by deepening roots can elevate carbonate weathering by 17%–207% (Wen et al., 2021). Carbonate weathering rates in heterogeneous and homogenous media can differ by more than an order of magnitude (Wen & Li, 2017, 2018). This relatively low impact of permeability contrasts could arise from several mechanisms. In previous studies (Wen & Li, 2017, 2018), carbonate dissolution only occurs in the low permeability zone, whereas in the current work carbonate and plagioclase occurs in both shallow and deep zones such that in effect only permeability heterogeneity existed. Physical heterogeneity alone has been shown to have limited impacts on mineral weathering (Jung & Navarre-Sitchler, 2018). In addition, the hillslope scale examined here is much larger in spatial scale than the pedon or meter scales, such that a longer transit time can promote carbonate weathering equilibrium.

The dependence of weathering on subsurface structure is also likely lithology-dependent and reflects the co-occurrence of carbonate and silicates. In shale-dominated sedimentary rocks, for example, oxidation of sulfides (e.g., pyrite) can produce acids and accelerate weathering (Bufe et al., 2021; Gu et al., 2020; Torres et al., 2014). Sulfide oxidation often occurs in deeper subsurface and is highly dependent on water table depth that regulates O_2 availability. Conditions that lead to deeper water tables have been observed to accelerate weathering in alpine mountains (Crawford et al., 2019). Shale weathering might have stronger dependence on subsurface structure than the lithology explored here. Vertical connectivity has also been shown to have much higher impact on silicate weathering without the presence of carbonates (Xiao et al., 2021). The fast carbonate reactions and the close-to-equilibrium conditions may be overwhelming such that it masks the effects of subsurface structure on silicate weathering.

WEN ET AL. 19 of 26



5.3. Stream Chemistry, Subsurface Structure, and Water Age

Numerical experiments show distinct depth profiles for different solutes. DOC concentrations generally decreased with depth, as organic carbon is less abundant and reactive at depth. In addition, DOC from shallow soils can continue to become mineralized at deeper depths. In contrast, concentrations of cations increased with depth (Figure 5), because of longer travel times, near-equilibrium conditions, or lower flow and export (Maher, 2011; Winnick & Maher, 2018). These different depth profiles led to distinct export patterns: DOC consistently shows flushing patterns with increasing concentration with discharge, whereas other solutes show consistent dilution patterns. This echoes observations in the literature that solute export patterns are shaped by their depth profiles (Stewart et al., 2022; Zhi & Li, 2020; Zhi et al., 2019).

Correspondingly, high DOC concentrations positively correlate with younger water fractions whereas other solutes positively correlate to older water (Figure 10). In particular, stream DOC exhibited more pronounced differences across flow regimes in HContrast with high permeability contrasts and lower vertical connectivity (Figure 10), which resembles observations in cations (Xiao et al., 2021). This alludes to the potential of establishing benchmark relationships between stream chemistry and subsurface structure characteristics such as permeability contrast and vertical connectivity. Stream chemistry has been used to infer shallow soil and deeper groundwater chemistry with satisfactory accuracy, especially for locations close to streams (Stewart et al., 2022). That is, the dynamics of stream chemistry may reveal subsurface structure such that we can use stream chemistry to mirror subsurface characteristics, infer reaction rates, and reveal structure-function relationships.

5.4. Model Assumption, Limitation, and Extrapolation Beyond Fitch

The model made several simplifications. The biogeochemical properties, including the abundance of organic matter and mineralogy, were kept constant. Neither do we consider topographic difference, for example, more OC in toeslopes than other positions. The rates of soil respiration do not include dependence on temperature and soil moisture, such that the rates represent "averages" across temperate and soil moisture conditions. Such choice permits differentiation among the effects of hydrological conditions and permeability contrasts without the confounding effects of soil moisture and temperature driving changes in soil CO₂ production.

The model also made simplifying assumptions for subsurface structure due to the lack of data. Permeability was assumed to decline with depth (Cardenas & Jiang, 2010). Although a common observation, permeability distribution can be complicated by the presence of fractures and roots that enable deeper penetration of acidic soil water and promote weathering at depth (Sullivan et al., 2022). This can happen especially when fractures are roots are the primary water conduits (Ackerer et al., 2021; Wen et al., 2021). The OC content typically declines with depth, as we assumed here (Hauser et al., 2020). This entails that maximum CO_2 production in shallow soil. Rates of OC respiration at depth however cannot be ignored (Soulet et al., 2021). For example, in an old-growth forest in Northern California (Tune et al., 2020), ~80% of CO_2 was produced from bedrock during the wet season; in the dry season, bedrock respiration continued but a greater fraction was emitted as soil CO_2 . These observations echo conclusions here and underscore the predominance of vertical CO_2 emission under dry conditions and lateral transport under wet conditions.

Note that the lack of subsurface structure and function data are common, as the subsurface characterization remains challenging and expensive. Except for a few Critical Zone Observatories (Brantley et al., 2017), subsurface structure and function have remained largely unknown. Detailed structural data, including images for fractures and root distributions, and functional data such as soil and groundwater chemistry and gas concentrations, are direly needed to reveal processes at depth and their connections to observed dynamics in surface water.

Despite model simplification and the model employment of Fitch idiosyncrasy, results here exhibit patterns similar to those observed in other places. For example, large-scale meta-analyses have indicated widespread CQ patterns (Botter et al., 2020; Ebeling et al., 2021). DOC exhibits flushing patterns in more than 90% of sites in the United States (Zarnetske et al., 2018). DIC and weathering-derived cations often exhibit dilution patterns (Bluth & Kump, 1994; Najjar et al., 2020). All these are similar to the model predictions here (Figure 6). In addition, soil $\rm CO_2$ has long been observed to increase with depth (Davidson & Trumbore, 1995; Fierer et al., 2005), which is consistent with depth profiles of solutes and soil $\rm CO_2$ from the model output here (Figures 4 and 5). Such consistency between data and model indicates the representation of key process dynamics. Under different

WEN ET AL. 20 of 26



climate, vegetation cover, and geology conditions, subsurface structure such as abundance of organic matter and permeability contrast will differ from Fitch site, which can lead to differing concentrations and fluxes. We however expect the general patterns and trends remain similar, as the key processes could remain similar.

6. Conclusions

We leverage a 2D hillslope reactive transport model to understand and quantify the rarely-explored linkages among flow paths, soil OC transformations, chemical weathering, and solute export across hydrological and subsurface structure gradients. The model integrates hydrological flow, solute transport, and biogeochemical reactions. The model was set up using measured discharge (i.e., precipitation – ET), water table depth, and soil properties (e.g., porosity and OC abundance). It was calibrated using soil CO_2 and soil water chemistry data from the Fitch Forest in Kansas (USA).

The results delineate a hillslope conceptual model that connects terrestrial carbon transformation and chemical weathering with vertical and lateral fluxes across gradients of hydrological conditions and subsurface permeability contrasts. Results demonstrate that dry conditions (0.08 mm/day) promoted deeper flow paths and longer water transit time, which enhanced carbon precipitation, production of inorganic carbon (IC, ~98% of OC), and vertical CO₂ export (~86% of produced IC); they also reduced DOC production and lateral carbon export. Conversely, storms (8.0 mm/day) promoted shallow flow and shorter water transit time, carbonate dissolution, DOC production, lateral carbon export, but reduced IC production (~88% of OC) and vertical carbon export (~53% of produced IC). Carbonate precipitated under dry conditions and dissolved under wet conditions as the fast flow drove the reaction to disequilibrium. Silicate weathering rates are not as sensitive to hydrological conditions because of its slower dissolution kinetics; its rates are higher under dry conditions with relatively high acidity. Permeability contrasts exert smaller influence on reaction rates than hydrological conditions but regulate the partitioning between water and solute fluxes via shallow and deeper flow paths. High permeability contrasts (low vertical connectivity) promote lateral fluxes. These results have important implications for understanding carbon production and export and chemical weathering under changing climate conditions.

Data Availability Statement

Data from this work are archived in the Consortium of Universities for the Advancement of Hydrologic Science, Inc. (CUAHSI) data website (https://www.hydroshare.org/resource/48991c1a1e14442a8f1ad98001469e29/). The link contains not only field data used in this work, but also simulation data. The simulation data include files for numerical experiments under the five discharge conditions in the three permeability contrast scenarios.

We acknowledge funding from the

National Natural Science Foundation of China (No. 42107234) and the US NSF Signals in the Soils (SitS; EAR-2026874, EAR-2012450, and EAR-2034232) and EAR-1911960. This work was also supported by Hatch funds (No. CA-R-ENS-5195-H, project accession No. 1022418) and a Signals in the Soils grant (No. 2021-67019-34341) from the USDA National Institute of Food and Agriculture. We acknowledge Ligia Souza and Soudeh Ghasemian for their assistance in measuring concentrations of extractable organic carbon and Morgan Okeson for installing piezometers and suction cup lysimeters and collecting water samples. We acknowledge National Ecological Observatory Network (NEON) and Natural Resources Conservation Service (NRCS) for their soil samples that informed this work. We are grateful to three anonymous reviewers and the editor for their insightful comments, which greatly improved this article.

Acknowledgments

References

Ackerer, J., Ranchoux, C., Lucas, Y., Viville, D., Clément, A., Fritz, B., et al. (2021). Investigating the role of deep weathering in critical zone evolution by reactive transport modeling of the geochemical composition of deep fracture water. *Geochimica et Cosmochimica Acta*, 312, 257–278. https://doi.org/10.1016/j.gca.2021.07.017

Ahrens, B., Braakhekke, M. C., Guggenberger, G., Schrumpf, M., & Reichstein, M. (2015). Contribution of sorption, DOC transport and microbial interactions to the C-14 age of a soil organic carbon profile: Insights from a calibrated process model. *Soil Biology and Biochemistry*, 88, 390–402. https://doi.org/10.1016/j.soilbio.2015.06.008

Andrews, J. A., & Schlesinger, W. H. (2001). Soil CO₂ dynamics, acidification, and chemical weathering in a temperate forest with experimental CO₂ enrichment. *Global Biogeochemical Cycles*, *15*(1), 149–162. https://doi.org/10.1029/2000gb001278

Ashok, K., & Sophocleous, M. (2008). Kansas geological survey.

Ault, T. R. (2020). On the essentials of drought in a changing climate. *Science*, 368(6488), 256–260. https://doi.org/10.1126/science.aaz5492
Barba, J., Cueva, A., Bahn, M., Barron-Gafford, G. A., Bond-Lamberty, B., Hanson, P. J., et al. (2018). Comparing ecosystem and soil respiration: Review and key challenges of tower-based and soil measurements. *Agricultural and Forest Meteorology*, 249, 434–443. https://doi.org/10.1016/j.agrformet.2017.10.028

Barnes, R. T., Butman, D. E., Wilson, H. F., & Raymond, P. A. (2018). Riverine export of aged carbon driven by flow path depth and residence time. *Environmental Science & Technology*, 52(3), 1028–1035. https://doi.org/10.1021/acs.est.7b04717

Batjes, N. H. (2014). Total carbon and nitrogen in the soils of the world. European Journal of Soil Science, 65(1), 10–21. https://doi.org/10.1111/ejss.12114_2

Battin, T. J., Luyssaert, S., Kaplan, L. A., Aufdenkampe, A. K., Richter, A., & Tranvik, L. J. (2009). The boundless carbon cycle. *Nature Geoscience*, 2(9), 598–600. https://doi.org/10.1038/ngeo618

Benettin, P., Bailey, S. W., Campbell, J. L., Green, M. B., Rinaldo, A., Likens, G. E., et al. (2015). Linking water age and solute dynamics in streamflow at the Hubbard Brook Experimental Forest, NH, USA. Water Resources Research, 51(11), 9256–9272. https://doi.org/10.1002/2015WR017552

WEN ET AL. 21 of 26



- Benettin, P., Fovet, O., & Li, L. (2020). Nitrate removal and young stream water fractions at the catchment scale. *Hydrological Processes*, 34(12), 2725–2738. https://doi.org/10.1002/hyp.13781
- Billings, S. A., Hirmas, D., Sullivan, P. L., Lehmeier, C. A., Bagchi, S., Min, K., et al. (2018). Loss of deep roots limits biogenic agents of soil development that are only partially restored by decades of forest regeneration. *Elementa-Science of the Anthropocene*, 6(34). https://doi.org/10.1525/elementa.287
- Bluth, G. J. S., & Kump, L. R. (1994). Lithoogic and climatologic controls of river chemistry. *Geochimica et Cosmochimica Acta*, 58(10), 2341–2359. https://doi.org/10.1016/0016-7037(94)90015-9
- Bond-Lamberty, B., Christianson, D. S., Malhotra, A., Pennington, S. C., Sihi, D., AghaKouchak, A., et al. (2020). COSORE: A community database for continuous soil respiration and other soil-atmosphere greenhouse gas flux data. *Global Change Biology*, 26(12), 7268–7283. https://doi.org/10.1111/gcb.15353
- Bond-Lamberty, B., & Thomson, A. (2010). A global database of soil respiration data. *Biogeosciences*, 7(6), 1915–1926. https://doi.org/10.5194/bg-7-1915-2010
- Botter, M., Li, L., Hartmann, J., Burlando, P., & Fatichi, S. (2020). Depth of solute generation is a dominant control on concentration-discharge relations. Water Resources Research, 56(8), e2019WR026695. https://doi.org/10.1029/2019wr026695
- Brantley, S. L., McDowell, W. H., Dietrich, W. E., White, T. S., Kumar, P., Anderson, S. P., et al. (2017). Designing a network of critical zone observatories to explore the living skin of the terrestrial Earth. Earth Surface Dynamics, 5(4), 841–860. https://doi.org/10.5194/esurf-5-841-2017
- Brookfield, A. E., Hansen, A. T., Sullivan, P. L., Czuba, J. A., Kirk, M. F., Li, L., et al. (2021). Predicting algal blooms: Are we overlooking groundwater? *Science of the Total Environment*, 769, 144442. https://doi.org/10.1016/j.scitotenv.2020.144442
- Brunsell, N. A., & Wilson, C. J. (2013). Multiscale interactions between water and carbon fluxes and environmental variables in a central US grassland. *Entropy*, 15(4), 1324–1341. https://doi.org/10.3390/e15041324
- Bufe, A., Hovius, N., Emberson, R., Rugenstein, J. K. C., Galy, A., Hassenruck-Gudipati, H. J., & Chang, J.-M. (2021). Co-variation of silicate, carbonate and sulfide weathering drives CO₂ release with erosion. *Nature Geoscience*, 14(4), 211–216. https://doi.org/10.1038/s41561-021-00714-3
- Buscot, F., & Varma, A. (2005). Microorganisms in soils: Roles in genesis and functions. Springer.
- Butman, D., Stackpoole, S., Stets, E., McDonald, C. P., Clow, D. W., & Striegl, R. G. (2016). Aquatic carbon cycling in the conterminous United States and implications for terrestrial carbon accounting. *Proceedings of the National Academy of Sciences*, 113(1), 58–63. https://doi.org/10.1073/pnas.1512651112
- Campeau, A., Bishop, K., Amvrosiadi, N., Billett, M. F., Garnett, M. N., Laudon, H., et al. (2019). Current forest carbon fixation fuels stream CO₂ emissions. *Nature Communications*, 10, 1876. https://doi.org/10.1038/s41467-019-09922-3
- Campeau, A., Wallin, M. B., Giesler, R., Löfgren, S., Mörth, C.-M., Schiff, S., et al. (2017). Multiple sources and sinks of dissolved inorganic carbon across Swedish streams, refocusing the lens of stable C isotopes. *Scientific Reports*, 7(1), 1–14. https://doi.org/10.1038/s41598-017-09049-9
- Cardenas, M. B., & Jiang, X.-W. (2010). Groundwater flow, transport, and residence times through topography-driven basins with exponentially decreasing permeability and porosity. Water Resources Research. 46(11). https://doi.org/10.1029/2010WR009370
- Carey, J. C., Tang, J., Templer, P. H., Kroeger, K. D., Crowther, T. W., Burton, A. J., et al. (2016). Temperature response of soil respiration largely unaltered with experimental warming. Proceedings of the National Academy of Sciences of the United States of America, 113(48), 13797–13802. https://doi.org/10.1073/pnas.1605365113
- Carman, P. C. (1997). Fluid flow through granular beds. Chemical Engineering Research and Design, 75, S32–S48. https://doi.org/10.1016/ S0263-8762(97)80003-2
- Chapin, F. S., Woodwell, G. M., Randerson, J. T., Rastetter, E. B., Lovett, G. M., Baldocchi, D. D., et al. (2006). Reconciling carbon-cycle concepts, terminology, and methods. *Ecosystems*, 9(7), 1041–1050. https://doi.org/10.1007/s10021-005-0105-7
- Clark, J. M., Bottrell, S. H., Evans, C. D., Monteith, D. T., Bartlett, R., Rose, R., et al. (2010). The importance of the relationship between scale and process in understanding long-term DOC dynamics. Science of the Total Environment, 408(13), 2768–2775. https://doi.org/10.1016/j.scitoteny.2010.02.046
- Clow, D. W., & Mast, M. A. (2010). Mechanisms for chemostatic behavior in catchments: Implications for CO₂ consumption by mineral weathering. Chemical Geology, 269(1–2), 40–51. https://doi.org/10.1016/j.chemgeo.2009.09.014
- Crawford, J. T., Hinckley, E.-L. S., Litaor, M. I., Brahney, J., & Neff, J. C. (2019). Evidence for accelerated weathering and sulfate export in high alpine environments. *Environmental Research Letters*, 14(12), 124092. https://doi.org/10.1088/1748-9326/ab5d9c
- Cueva, A., Volkmann, T. H. M., van Haren, J., Troch, P. A., & Meredith, L. K. (2019). Reconciling negative soil CO₂ fluxes: Insights from a large-scale experimental hillslope. Soil Systems, 3(1), 10. https://doi.org/10.3390/soilsystems3010010
- Davidson, E. A., & Trumbore, S. E. (1995). Gas diffusivity and production of CO₂ in deep soils of the eastern Amazon. *Tellus B: Chemical and Physical Meteorology*, 47(5), 550–565. https://doi.org/10.3402/tellusb.v47i5.16071
- Deng, H., Voltolini, M., Molins, S., Steefel, C., DePaolo, D., Ajo-Franklin, J., & Yang, L. (2017). Alteration and erosion of rock matrix bordering a carbonate-rich shale fracture. Environmental Science & Technology, 51(15), 8861–8868. https://doi.org/10.1021/acs.est.7b02063
- Dickey, H. P., Zimmerman, J. L., Plinsky, R. O., & Davis, R. D. (1977). Soil survey of Douglas County, Kansas.
- Druhan, J. L., Lawrence, C. R., Covey, A. K., Giannetta, M. G., & Oster, J. L. (2021). A reactive transport approach to modeling cave seepage water chemistry I: Carbon isotope transformations. Geochimica et Cosmochimica Acta. https://doi.org/10.1016/j.gca.2021.06.041
- Duvert, C., Butman, D. E., Marx, A., Ribolzi, O., & Hutley, L. B. (2018). CO₂ evasion along streams driven by groundwater inputs and geomorphic controls. *Nature Geoscience*, 11(11), 813–818. https://doi.org/10.1038/s41561-018-0245-y
- Duvert, C., Hutley, L. B., Birkel, C., Rudge, M., Munksgaard, N. C., Wynn, J. G., et al. (2020). Seasonal shift from biogenic to geogenic fluvial carbon caused by changing water sources in the wet-dry tropics. *Journal of Geophysical Research: Biogeosciences*, 125(2), e2019JG005384. https://doi.org/10.1029/2019JG005384
- Dwivedi, D., Steefel, C. I., Arora, B., Banfield, J., Bargar, J., Boyanov, M. I., et al. (2022). From legacy contamination to watershed systems science: A review of scientific insights and technologies developed through DOE-supported research in water and energy security. Environmental Research Letters, 17(4), 043004. https://doi.org/10.1088/1748-9326/ac59a9
- Ebeling, P., Kumar, R., Weber, M., Knoll, L., Fleckenstein, J. H., & Musolff, A. (2021). Archetypes and controls of riverine nutrient export across German catchments. Water Resources Research, 57(4), e2020WR028134. https://doi.org/10.1029/2020WR028134
- Ekblad, A., & Högberg, P. (2001). Natural abundance of ¹³C in CO₂ respired from forest soils reveals speed of link between tree photosynthesis and root respiration. *Oecologia*, 127(3), 305–308. https://doi.org/10.1007/s004420100667
- Elhakim, A. F. (2016). Estimation of soil permeability. Alexandria Engineering Journal, 55(3), 2631–2638. https://doi.org/10.1016/j.aej.2016.07.034

WEN ET AL. 22 of 26



- Fang, C., & Moncrieff, J. (2001). The dependence of soil CO₂ efflux on temperature. Soil Biology and Biochemistry, 33(2), 155–165. https://doi.org/10.1016/s0038-0717(00)00125-5
- Fierer, N., Chadwick, O. A., & Trumbore, S. E. (2005). Production of CO₂ in soil profiles of a California annual grassland. *Ecosystems*, 8(4), 412–429. https://doi.org/10.1007/s10021-003-0151-y
- Fitch, H. S. (2006). Ecological succession on a natural area in northeastern Kansas from 1948 to 2006. *Herpetological Conservation and Biology*, 1(1), 1–5.
- Foth, H. D. (1978). Fundamentals of soil science. Soil Science, 125(4), 272. https://doi.org/10.1097/00010694-197804000-00021
- Gleeson, T., Befus, K. M., Jasechko, S., Luijendijk, E., & Cardenas, M. B. (2016). The global volume and distribution of modern groundwater. Nature Geoscience, 9(2), 161. https://doi.org/10.1038/ngeo2590
- Golubev, S. V., Pokrovsky, O. S., & Schott, J. (2005). Experimental determination of the effect of dissolved CO₂ on the dissolution kinetics of Mg and Ca silicates at 25°C. Chemical Geology, 217(3), 227–238. https://doi.org/10.1016/j.chemgeo.2004.12.011
- Gómez-Gener, L., Lupon, A., Laudon, H., & Sponseller, R. A. (2020). Drought alters the biogeochemistry of boreal stream networks. *Nature Communications*, 11(1), 1795. https://doi.org/10.1038/s41467-020-15496-2
- Grimm, N. B., Gergel, S. E., McDowell, W. H., Boyer, E. W., Dent, C. L., Groffman, P., et al. (2003). Merging aquatic and terrestrial perspectives of nutrient biogeochemistry. *Oecologia*, 137(4), 485–501. https://doi.org/10.1007/s00442-003-1382-5
- Gu, X., Heaney, P. J., Reis, F., & Brantley, S. L. (2020). Deep abiotic weathering of pyrite. Science, 370(6515), 425. https://doi.org/10.1126/science.abb8092
- Hanson, P. J., Edwards, N. T., Garten, C. T., & Andrews, J. A. (2000). Separating root and soil microbial contributions to soil respiration: A review of methods and observations. Biogeochemistry, 48(1), 115–146. https://doi.org/10.1023/a:1006244819642
- Harman, C., & Sivapalan, M. (2009). Effects of hydraulic conductivity variability on hillslope-scale shallow subsurface flow response and storage-discharge relations. Water Resources Research, 45(1). https://doi.org/10.1029/2008WR007228
- Harman, C. J., & Cosans, C. L. (2019). A low-dimensional model of bedrock weathering and lateral flow coevolution in hillslopes: 2. Controls on weathering and permeability profiles, drainage hydraulics, and solute export pathways. *Hydrological Processes*, 33(8), 1168–1190. https://doi.org/10.1002/hyp.13385
- Hauser, E., Richter, D. D., Markewitz, D., Brecheisen, Z., & Billings, S. A. (2020). Persistent anthropogenic legacies structure depth dependence of regenerating rooting systems and their functions. *Biogeochemistry*, 147(3), 259–275. https://doi.org/10.1007/s10533-020-00641-2
- Heidari, P., Li, L., Jin, L., Williams, J. Z., & Brantley, S. L. (2017). A reactive transport model for Marcellus shale weathering. Geochimica et Cosmochimica Acta, 217(Supplement C), 421–440. https://doi.org/10.1016/j.gca.2017.08.011
- Heinemeyer, A., Hartley, I. P., Evans, S. P., Carreira De La Fuente, J. A., & Ineson, P. (2007). Forest soil CO₂ flux: Uncovering the contribution and environmental responses of ectomycorrhizas. *Global Change Biology*, 13(8), 1786–1797. https://doi.org/10.1111/j.1365-2486.2007.01383.x
- Herbert, B. E., & Bertsch, P. M. (1995). Characterization of dissolved and colloidal organic matter in soil solution: A review. *Carbon forms and functions in forest soils* (pp. 63–88).
- Horgby, Å., Boix Canadell, M., Ulseth, A. J., Vennemann, T. W., & Battin, T. J. (2019). High-resolution spatial sampling identifies groundwater as driver of CO₂ dynamics in an alpine stream network. *Journal of Geophysical Research: Biogeosciences*, 124(7), 1961–1976. https://doi. org/10.1029/2019JG005047
- Horgby, Å., Gómez-Gener, L., Escoffier, N., & Battin, T. J. (2019). Dynamics and potential drivers of CO₂ concentration and evasion across temporal scales in high-alpine streams. Environmental Research Letters, 14(12), 124082. https://doi.org/10.1088/1748-9326/ab5cb8
- Hotchkiss, E. R., Hall, R. O., Sponseller, R. A., Butman, D., Klaminder, J., Laudon, H., et al. (2015). Sources of and processes controlling CO₂ emissions change with the size of streams and rivers. *Nature Geoscience*, 8(9), 696. https://doi.org/10.1038/ngeo2507
- Jian, J., Vargas, R., Anderson-Teixeira, K., Stell, E., Herrmann, V., Horn, M., et al. (2021). A restructured and updated global soil respiration database (SRDB-V5). Earth System Science Data, 13(2), 255–267. https://doi.org/10.5194/essd-13-255-2021
- Jin, L. X., Ravella, R., Ketchum, B., Bierman, P. R., Heaney, P., White, T., & Brantley, S. L. (2010). Mineral weathering and elemental transport during hillslope evolution at the Susquehanna/Shale Hills Critical Zone Observatory. Geochimica et Cosmochimica Acta, 74(13), 3669–3691. https://doi.org/10.1016/j.gca.2010.03.036
- Jobbagy, E. G., & Jackson, R. B. (2000). The vertical distribution of soil organic carbon and its relation to climate and vegetation. *Ecological Applications*, 10(2), 423–436. https://doi.org/10.1890/1051-0761(2000)010[0423:tvdoso]2.0.co;2
- Jones, D. L., Hodge, A., & Kuzyakov, Y. (2004). Plant and mycorrhizal regulation of rhizodeposition. New Phytologist, 163(3), 459-480.
- Jung, H., & Navarre-Sitchler, A. (2018). Physical heterogeneity control on effective mineral dissolution rates. Geochimica et Cosmochimica Acta, 227, 246–263. https://doi.org/10.1016/j.gca.2018.02.028
- Keller, C. K. (2019). Carbon exports from terrestrial ecosystems: A critical-zone framework. *Ecosystems*, 22(8), 1691–1705. https://doi.org/10.1007/s10021-019-00375-9
- Kuzyakov, Y. (2006). Sources of CO₂ efflux from soil and review of partitioning methods. *Soil Biology and Biochemistry*, 38(3), 425–448. https://doi.org/10.1016/j.soilbio.2005.08.020
- Lawrence, C., Harden, J., & Maher, K. (2014). Modeling the influence of organic acids on soil weathering. *Geochimica et Cosmochimica Acta*, 139, 487–507. https://doi.org/10.1016/j.gca.2014.05.003
- Li, L., Bao, C., Sullivan, P. L., Brantley, S., Shi, Y., & Duffy, C. (2017). Understanding watershed hydrogeochemistry: 2. Synchronized hydrological and geochemical processes drive stream chemostatic behavior. Water Resources Research, 53(3), 2346–2367. https://doi.org/10.1002/2016wr018935
- Li, L., Maher, K., Navarre-Sitchler, A., Druhan, J., Meile, C., Lawrence, C., et al. (2017). Expanding the role of reactive transport models in critical zone processes. Earth-Science Reviews, 165, 280–301. https://doi.org/10.1016/j.earscirev.2016.09.001
- Li, L., Steefel, C. I., Kowalsky, M. B., Englert, A., & Hubbard, S. S. (2010). Effects of physical and geochemical heterogeneities on mineral transformation and biomass accumulation during biostimulation experiments at Rifle, Colorado. *Journal of Contaminant Hydrology*, 112(1–4), 45–63. https://doi.org/10.1016/j.jconhyd.2009.10.006
- Li, L., Stewart, B., Zhi, W., Sadayappan, K., Ramesh, S., Kerins, D., et al. (2022). Climate controls on river chemistry. *Earth's Future*, 10(6), e2021EF002603. https://doi.org/10.1029/2021EF002603
- Li, L., Sullivan, P. L., Benettin, P., Cirpka, O. A., Bishop, K., Brantley, S. L., et al. (2021). Toward catchment hydro-biogeochemical theories. WIREs Water, e1495. https://doi.org/10.1002/wat2.1495
- Liu, Z., Macpherson, G. L., Groves, C., Martin, J. B., Yuan, D., & Zeng, S. (2018). Large and active CO₂ uptake by coupled carbonate weathering. Earth-Science Reviews, 182, 42–49. https://doi.org/10.1016/j.earscirev.2018.05.007
- Liu, Z. H., Dreybrodt, W., & Wang, H. J. (2010). A new direction in effective accounting for the atmospheric CO₂ budget: Considering the combined action of carbonate dissolution, the global water cycle and photosynthetic uptake of DIC by aquatic organisms. *Earth-Science Reviews*, 99(3–4), 162–172. https://doi.org/10.1016/j.earscirev.2010.03.001

WEN ET AL. 23 of 26



- Lloyd, J., & Taylor, J. A. (1994). On the temperature dependence of soil respiration. Functional Ecology, 8(3), 315–323. https://doi.org/10.2307/2389824
- Ma, J., Liu, R., Tang, L. S., Lan, Z. D., & Li, Y. (2014). A downward CO₂ flux seems to have nowhere to go. *Biogeosciences*, 11(22), 6251–6262. https://doi.org/10.5194/bg-11-6251-2014
- Macpherson, G. L. (2009). CO₂ distribution in groundwater and the impact of groundwater extraction on the global C cycle. *Chemical Geology*, 264(1), 328–336. https://doi.org/10.1016/j.chemgeo.2009.03.018
- Maher, K. (2011). The role of fluid residence time and topographic scales in determining chemical fluxes from landscapes. Earth and Planetary Science Letters, 312(1-2), 48-58. https://doi.org/10.1016/j.epsl.2011.09.040
- Maher, K., Steefel, C. I., DePaolo, D. J., & Viani, B. E. (2006). The mineral dissolution rate conundrum: Insights from reactive transport modeling of U isotopes and pore fluid chemistry in marine sediments. *Geochimica et Cosmochimica Acta*, 70(2), 337–363. https://doi.org/10.1016/j. gca.2005.09.001
- Mastrotheodoros, T., Pappas, C., Molnar, P., Burlando, P., Manoli, G., Parajka, J., et al. (2020). More green and less blue water in the Alps during warmer summers. *Nature Climate Change*, 10(2), 155–161. https://doi.org/10.1038/s41558-019-0676-5
- McElwee, C. D., Butler, J. J., Jr., Macpherson, G. L., Bohling, G. C., & Miller, R. D. (1995). Characterization of heterogeneities controlling transport and fate of pollutants in unconsolidated sand and gravel aquifers. Kansas State Geological Survey.
- Michelsen, A., Andersson, M., Jensen, M., Kjoller, A., & Gashew, M. (2004). Carbon stocks, soil respiration and microbial biomass in fire-prone tropical grassland, woodland and forest ecosystems. Soil Biology and Biochemistry, 36(11), 1707–1717. https://doi.org/10.1016/j. soilbio.2004.04.028
- Monger, H. C., Kraimer, R. A., Khresat, S. e., Cole, D. R., Wang, X., & Wang, J. (2015). Sequestration of inorganic carbon in soil and ground-water. Geology, 43(5), 375–378. https://doi.org/10.1130/g36449.1
- Moriasi, D. N., Arnold, J. G., Van Liew, M. W., Bingner, R. L., Harmel, R. D., & Veith, T. L. (2007). Model evaluation guidelines for systematic quantification of accuracy in watershed simulations. *Transactions of the ASABE*, 50(3), 885–900. https://doi.org/10.13031/2013.23153
- Mulholland, P. J. (1997). Dissolved organic matter concentration and flux in streams. *Journal of the North American Benthological Society*, 16(1), 131–141. https://doi.org/10.2307/1468246
- Murphy, B. W., Wilson, B. R., & Koen, T. (2019). Mathematical functions to model the depth distribution of soil organic carbon in a range of soils from New South Wales, Australia under different land uses. Soil Systems, 3(3). https://doi.org/10.3390/soilsystems3030046
- Najjar, R. G., Herrmann, M., Cintrón Del Valle, S. M., Friedman, J. R., Friedrichs, M. A. M., Harris, L. A., et al. (2020). Alkalinity in tidal tributaries of the Chesapeake Bay. *Journal of Geophysical Research: Oceans*, 125(1). https://doi.org/10.1029/2019jc015597
- Olshansky, Y., Knowles, J. F., Barron-Gafford, G. A., Rasmussen, C., Abramson, N., & Chorover, J. (2019). Soil fluid biogeochemical response to climatic events. *Journal of Geophysical Research: Biogeosciences*, 124(9), 2866–2882. https://doi.org/10.1029/2019JG005216
- Oren, A., & Chefetz, B. (2012). Sorptive and desorptive fractionation of dissolved organic matter by mineral soil matrices. *Journal of Environmental Quality*, 41(2), 526–533. https://doi.org/10.2134/jeg2011.0362
- Pabich, W. J., Valiela, I., & Hemond, H. F. (2001). Relationship between DOC concentration and vadose zone thickness and depth below water table in groundwater of Cape Cod, USA. *Biogeochemistry*, 55(3), 247–268. https://doi.org/10.1023/a:1011842918260
- Palandri, J. L., & Kharaka, Y. K. (2004). A compilation of rate parameters of water-mineral interaction kinetics for application to geochemical modeling. Geological Survey.
- Penman, D. E., Caves Rugenstein, J. K., Ibarra, D. E., & Winnick, M. J. (2020). Silicate weathering as a feedback and forcing in Earth's climate and carbon cycle. Earth-Science Reviews, 209, 103298. https://doi.org/10.1016/j.earscirev.2020.103298
- Piney, G., Bernal, S., Abbott, B. W., Lupon, A., Marti, E., Sabater, F., & Krause, S. (2018). Riparian corridors: A new conceptual framework for assessing nitrogen buffering across biomes. Frontiers in Environmental Science, 6. https://doi.org/10.3389/fenvs.2018.00047
- Plummer, L., Wigley, T., & Parkhurst, D. (1978). The kinetics of calcite dissolution in CO₂-water systems at 5 degrees to 60 degrees C and 0.0 to 1.0 atm CO₂. American Journal of Science, 278(2), 179–216. https://doi.org/10.2475/ajs.278.2.179
- Raich, J. W., & Schlesinger, W. H. (1992). The global carbon dioxide flux in soil respiration and its relationship to vegetation and climate. *Tellus B: Chemical and Physical Meteorology*, 44(2), 81–99. https://doi.org/10.1034/j.1600-0889.1992.t01-1-00001.x
- Ransom, M. D., Rice, C. W., Todd, T. C., & Wehmueller, W. A. (1998). Soils and soil biota: Grassland dynamics: Long-term ecological research in tallgrass prairie. Long-term ecological research network series. Oxford University Press.
- Rawls, W. J., Gimenez, D., & Grossman, R. (1998). Use of soil texture, bulk density, and slope of the water retention curve to predict saturated hydraulic conductivity. *Transactions of the ASAE*, 41(4), 983–988. https://doi.org/10.13031/2013.17270
- Raymond, P. A., Hartmann, J., Lauerwald, R., Sobek, S., McDonald, C., Hoover, M., et al. (2013). Global carbon dioxide emissions from inland waters. *Nature*, 503(7476), 355–359. https://doi.org/10.1038/nature12760
- Raymond, P. A., & Saiers, J. E. (2010). Event controlled DOC export from forested watersheds. *Biogeochemistry*, 100(1), 197–209. https://doi.org/10.1007/s10533-010-9416-7
- Regnier, P., Friedlingstein, P., Ciais, P., Mackenzie, F. T., Gruber, N., Janssens, I. A., et al. (2013). Anthropogenic perturbation of the carbon fluxes from land to ocean. *Nature Geoscience*, 6(8), 597–607. https://doi.org/10.1038/ngeo1830
- Richter, D. D., & Billings, S. A. (2015). 'One physical system': Tansley's ecosystem as Earth's critical zone. New Phytologist, 206(3), 900–912. https://doi.org/10.1111/nph.13338
- Riley, W., Maggi, F., Kleber, M., Torn, M., Tang, J., Dwivedi, D., & Guerry, N. (2014). Long residence times of rapidly decomposable soil organic matter: Application of a multi-phase, multi-component, and vertically resolved model (BAMS1) to soil carbon dynamics. *Geoscientific Model Development*, 7(4). https://doi.org/10.5194/gmd-7-1335-2014
- Saar, M. O., & Manga, M. (2004). Depth dependence of permeability in the Oregon Cascades inferred from hydrogeologic, thermal, seismic, and magmatic modeling constraints. *Journal of Geophysical Research*, 109(B4). https://doi.org/10.1029/2003JB002855
- Sagi, N., Zaguri, M., & Hawlena, D. (2021). Soil CO₂ influx in drylands: A conceptual framework and empirical examination. Soil Biology and Biochemistry, 156, 108209. https://doi.org/10.1016/j.soilbio.2021.108209
- Schlesinger, W. H. (1982). Carbon storage in the caliche of arid soils: A case study from Arizona. Soil Science, 133(4), 247–255. https://doi.org/10.1097/00010694-198204000-00008
- Schlesinger, W. H., & Amundson, R. (2019). Managing for soil carbon sequestration: Let's get realistic. Global Change Biology, 25(2), 386–389. https://doi.org/10.1111/gcb.14478
- Schlesinger, W. H., Belnap, J., & Marion, G. (2009). On carbon sequestration in desert ecosystems. *Global Change Biology*, 15(6), 1488–1490. https://doi.org/10.1111/j.1365-2486.2008.01763.x
- Seibert, J., Grabs, T., Köhler, S., Laudon, H., Winterdahl, M., & Bishop, K. (2009). Linking soil- and stream-water chemistry based on a Riparian flow-concentration integration model. *Hydrology and Earth System Sciences*, 13(12), 2287–2297. https://doi.org/10.5194/hess-13-2287-2009 Soil Survery Staff. (2010). *Keys to soil taxonomy*. Natural Resources Conservation Service (US), United States Department of Agriculture.

WEN ET AL. 24 of 26



- Soil Survery Staff. (2022). Web soil survey, edited. Natural Resources Conservation Service, United States Department of Agriculture. Retrieved from http://websoilsurvey.sc.egov.usda.gov/
- Soper, F. M., McCalley, C. K., Sparks, K., & Sparks, J. P. (2017). Soil carbon dioxide emissions from the Mojave desert: Isotopic evidence for a carbonate source. Geophysical Research Letters, 44(1), 245–251. https://doi.org/10.1002/2016GL071198
- Sorenson, P. T., Quideau, S. A., Rivard, B., & Dyck, M. (2020). Distribution mapping of soil profile carbon and nitrogen with laboratory imaging spectroscopy. Geoderma, 359. https://doi.org/10.1016/j.geoderma.2019.113982
- Soulet, G., Hilton, R. G., Garnett, M. H., Roylands, T., Klotz, S., Croissant, T., et al. (2021). Temperature control on CO₂ emissions from the weathering of sedimentary rocks. *Nature Geoscience*, 14(9), 665–671. https://doi.org/10.1038/s41561-021-00805-1
- Sprenger, M., Tetzlaff, D., Buttle, J., Laudon, H., Leistert, H., Mitchell, C. P. J., et al. (2018). Measuring and modeling stable isotopes of mobile and bulk soil water. *Vadose Zone Journal*, 17(1). https://doi.org/10.2136/vzj2017.08.0149
- Stanbery, C. A., Pierce, J. L., Benner, S. G., & Lohse, K. (2017). On the rocks: Quantifying storage of inorganic soil carbon on gravels and determining pedon-scale variability. Catena, 157, 436–442. https://doi.org/10.1016/j.catena.2017.06.011
- Steefel, C. I., Appelo, C. A. J., Arora, B., Jacques, D., Kalbacher, T., Kolditz, O., et al. (2015). Reactive transport codes for subsurface environmental simulation. Computational Geosciences, 19(3), 445–478. https://doi.org/10.1007/s10596-014-9443-x
- Stewart, B., Shanley, J. B., Kirchner, J. W., Norris, D., Adler, T., Bristol, C., et al. (2022). Streams as mirrors: Reading subsurface water chemistry from stream chemistry. *Water Resources Research*, 58(1), e2021WR029931. https://doi.org/10.1029/2021WR029931
- Subke, J.-A., Inglima, I., & Cotrufo, M. F. (2006). Trends and methodological impacts in soil CO₂ efflux partitioning: A metaanalytical review. Global Change Biology, 12(6), 921–943. https://doi.org/10.1111/j.1365-2486.2006.01117.x
- Sullivan, P. L., Billings, S. A., Hirmas, D., Li, L., Zhang, X., Ziegler, S., et al. (2022). Embracing the dynamic nature of soil structure: A paradigm illuminating the role of life in critical zones of the Anthropocene. *Earth-Science Reviews*, 225, 103873. https://doi.org/10.1016/j.earscirey.2021.103873
- Sullivan, P. L., Stops, M. W., Macpherson, G. L., Li, L., Hirmas, D. R., & Dodds, W. K. (2019). How landscape heterogeneity governs stream water concentration-discharge behavior in carbonate terrains (Konza Prairie, USA). Chemical Geology, 527, 118989. https://doi.org/10.1016/j.chemgeo.2018.12.002
- Tank, S. E., Fellman, J. B., Hood, E., & Kritzberg, E. S. (2018). Beyond respiration: Controls on lateral carbon fluxes across the terrestrial-aquatic interface. Limnology and Oceanography Letters, 3(3), 76–88. https://doi.org/10.1002/lo12.10065
- Tipper, E. T., Bickle, M. J., Galy, A., West, A. J., Pomies, C., & Chapman, H. J. (2006). The short term climatic sensitivity of carbonate and silicate weathering fluxes: Insight from seasonal variations in river chemistry. *Geochimica et Cosmochimica Acta*, 70(11), 2737–2754. https://doi.org/10.1016/j.gca.2006.03.005
- Torres, M. A., & Baronas, J. J. (2021). Modulation of riverine concentration-discharge relationships by changes in the shape of the water transit time distribution. Global Biogeochemical Cycles, 35(1), e2020GB006694. https://doi.org/10.1029/2020GB006694
- Torres, M. A., West, A. J., & Li, G. J. (2014). Sulphide oxidation and carbonate dissolution as a source of CO₂ over geological timescales. *Nature*, 507(7492), 346. https://doi.org/10.1038/nature13030
- Tune, A. K., Druhan, J. L., Wang, J., Bennett, P. C., & Rempe, D. M. (2020). Carbon dioxide production in bedrock beneath soils substantially contributes to forest carbon cycling. *Journal of Geophysical Research: Biogeosciences*, 125(12), e2020JG005795. https://doi.org/10.1029/2020JG005795
- Vasconcelos, S. S., Zarin, D. J., Capanu, M., Littell, R., Davidson, E. A., Ishida, F. Y., et al. (2004). Moisture and substrate availability constrain soil trace gas fluxes in an eastern Amazonian regrowth forest. *Global Biogeochemical Cycles*, 18(2).
- Wan, J., Tokunaga, T. K., Williams, K. H., Dong, W., Brown, W., Henderson, A. N., et al. (2019). Predicting sedimentary bedrock subsurface weathering fronts and weathering rates. *Scientific Reports*, 9(1), 17198. https://doi.org/10.1038/s41598-019-53205-2
- Wang, G. S., Jagadamma, S., Mayes, M. A., Schadt, C. W., Steinweg, J. M., Gu, L. H., & Post, W. M. (2015). Microbial dormancy improves development and experimental validation of ecosystem model. *The ISME Journal*, 9(1), 226–237. https://doi.org/10.1038/ismej.2014.120
- Welch, L. A., & Allen, D. M. (2014). Hydraulic conductivity characteristics in mountains and implications for conceptualizing bedrock ground-water flow. *Hydrogeology Journal*, 22(5), 1003–1026. https://doi.org/10.1007/s10040-014-1121-5
- Wen, H., & Li, L. (2017). An upscaled rate law for magnesite dissolution in heterogeneous porous media. *Geochimica et Cosmochimica Acta*, 210, 289–305. https://doi.org/10.1016/j.gca.2017.04.019
- Wen, H., & Li, L. (2018). An upscaled rate law for mineral dissolution in heterogeneous media: The role of time and length scales. *Geochimica et Cosmochimica Acta*, 235, 1–20. https://doi.org/10.1016/j.gca.2018.04.024
- Wen, H., Perdrial, J., Abbott, B. W., Bernal, S., Dupas, R., Godsey, S. E., et al. (2020). Temperature controls production but hydrology regulates export of dissolved organic carbon at the catchment scale. *Hydrology and Earth System Sciences*, 24(2), 945–966. https://doi.org/10.5194/hess-24-945-2020
- Wen, H., Sullivan, P. L., Macpherson, G. L., Billings, S. A., & Li, L. (2021). Deepening roots can enhance carbonate weathering by amplifying CO₂-rich recharge. *Biogeosciences*, 18(1), 55–75. https://doi.org/10.5194/bg-18-55-2021
- West, A. J., Galy, A., & Bickle, M. (2005). Tectonic and climatic controls on silicate weathering. Earth and Planetary Science Letters, 235(1–2), 211–228. https://doi.org/10.1016/j.epsl.2005.03.020
- White, A. F., & Blum, A. E. (1995). Effects of climate on chemical, weathering in watersheds. *Geochimica et Cosmochimica Acta*, 59(9), 1729–1747. https://doi.org/10.1016/0016-7037(95)00078-E
- Whittemore, D. O., Macfarlane, P. A., & Wilson, B. B. (2014). Water resources of the Dakota Aquifer in Kansas. Citeseer.
- Winnick, M. J., & Maher, K. (2018). Relationships between CO₂, thermodynamic limits on silicate weathering, and the strength of the silicate weathering feedback. *Earth and Planetary Science Letters*, 485, 111–120. https://doi.org/10.1016/j.epsl.2018.01.005
- Wolery, T. J., Jackson, K. J., Bourcier, W. L., Bruton, C. J., Viani, B. E., Knauss, K. G., & Delany, J. M. (1990). Current status of the eq3/6 software package for geochemical modeling. ACS Symposium Series, 416, 104–116. <Go to ISI>://WOS:A1990CM60900008. https://doi.org/10.1021/bk-1990-0416.ch008
- Worrall, F., Burt, T., & Adamson, J. (2004). Can climate change explain increases in DOC flux from upland peat catchments? *Science of the Total Environment*, 326(1), 95–112. https://doi.org/10.1016/j.scitotenv.2003.11.022
- Worrall, F., Burt, T. P., & Adamson, J. (2008). Long-term records of dissolved organic carbon flux from peat-covered catchments: Evidence for a drought effect? *Hydrological Processes*, 22(16), 3181–3193. https://doi.org/10.1002/hyp.6907
- Xiao, D., Brantley, S. L., & Li, L. (2021). Vertical connectivity regulates water transit time and chemical weathering at the hillslope scale. Water Resources Research, 57(8), e2020WR029207. https://doi.org/10.1029/2020WR029207
- Yan, Z. F., Bond-Lamberty, B., Todd-Brown, K. E., Bailey, V. L., Li, S. L., Liu, C. Q., & Liu, C. X. (2018). A moisture function of soil heter-otrophic respiration that incorporates microscale processes. *Nature Communications*, 9, 2562. https://doi.org/10.1038/s41467-018-04971-6

WEN ET AL. 25 of 26



- Zamanian, K., Pustovoytov, K., & Kuzyakov, Y. (2016). Pedogenic carbonates: Forms and formation processes. *Earth-Science Reviews*, 157, 1–17. https://doi.org/10.1016/j.earscirev.2016.03.003
- Zarnetske, J. P., Bouda, M., Abbott, B. W., Saiers, J., & Raymond, P. A. (2018). Generality of hydrologic transport limitation of water-shed organic carbon flux across Ecoregions of the United States. *Geophysical Research Letters*, 45(21), 11702–711711. https://doi.org/10.1029/2018g1080005
- Zeng, S., Liu, Z., & Kaufmann, G. (2019). Sensitivity of the global carbonate weathering carbon-sink flux to climate and land-use changes. *Nature Communications*, 10(1), 5749. https://doi.org/10.1038/s41467-019-13772-4
- Zhi, W., & Li, L. (2020). The shallow and deep hypothesis: Subsurface vertical chemical contrasts shape nitrate export patterns from different land uses. *Environmental Science & Technology*, 54(19), 11915–11928. https://doi.org/10.1021/acs.est.0c01340
- Zhi, W., Li, L., Dong, W., Brown, W., Kaye, J., Steefel, C., & Williams, K. H. (2019). Distinct source water chemistry shapes contrasting concentration-discharge patterns. Water Resources Research. https://doi.org/10.1029/2018WR024257
- Zhong, J., Li, S. L., Tao, F. X., Yue, F. J., & Liu, C. Q. (2017). Sensitivity of chemical weathering and dissolved carbon dynamics to hydrological conditions in a typical karst river. *Scientific Reports*, 7, 42944. https://doi.org/10.1038/srep42944

WEN ET AL. 26 of 26